

Cloud-cloud collision in S235: triggered the formation of high-mass stars and young star clusters

En Chen,^{1,2*} Yu Gao,^{1,3} Shiyu Zhang,¹ Xuepeng Chen,¹ Min Fang,¹ Qianru He^{1,2} Xuejian Jiang,⁴
Yan Sun,¹ Xiaolong Wang,¹ and Hongjun Ma¹

¹Purple Mountain Observatory & Key Laboratory of Radio Astronomy, No.10 Yuanhua Road, Nanjing, 210034, People's Republic of China

²University of Science and Technology of China, No.96 Jinzhai Road, Hefei, 230026, People's Republic of China

³Department of Astronomy, Xiamen University, No.422 Siming South Road, Xiamen, Fujian, 361005, People's Republic of China

⁴Research Center for Intelligent Computing Platforms, Zhejiang Laboratory, Hangzhou, 311100, People's Republic of China

Accepted 2023 November 6. Received 2023 November 2; in original form 2023 May 19.

ABSTRACT

We present the analysis of cloud-cloud collision (CCC) process in the Galactic molecular complex S235. Our new CO observations performed with the PMO-13.7m telescope reveal two molecular clouds, namely the S235-Main and the S235-ABC, with ~ 4 km s⁻¹ velocity separation. The bridge feature, the possible colliding interface and the complementary distribution of the two clouds are significant observational signatures of cloud-cloud collision in S235. The most direct evidence of cloud-cloud collision process in S235 is that the S235-Main (in a distance of 1547^{+44}_{-43} pc) and S235-ABC (1567^{+33}_{-39} pc) meet at almost the same position (within 1σ error range) at a supersonic relative speed. We identified ten ¹³CO clumps from PMO-13.7m observations, 22 dust cores from the archival SCUBA-2 data, and 550 YSOs from NIR-MIR data. 63% of total YSOs are clustering in seven MST groups (M1–M7). The tight association between the YSO groups (M1 & M7) and the bridge feature suggests that the CCC process triggers star formation there. The collisional impact subregion (the South) shows 3 ~ 5 times higher CFE and SFE (average value of 12.3% and 10.6%, respectively) than the non-collisional impact subregion (2.4% and 2.6%, respectively), suggesting that the CCC process may have enhanced the CFE and SFE of the clouds compared to those without collision influence.

Key words: ISM: clouds – ISM: individual objects (S235) – stars: formation – stars: pre-main sequence

1 INTRODUCTION

Star formation activity is one of the most fundamental processes controlling galactic evolution. Stars are believed to be born from dense molecular gas. A tight correlation between the mass of dense molecular gas and the star formation rate (SFR) was found by Gao & Solomon (2004), known as the law of star formation (or the Kennicutt-Schmidt relation (Kennicutt 1998)). In recent theories, the star formation process is thought to be due to gravitational instability in a turbulent molecular cloud that causes the cloud to collapse and thus form stars (McKee & Ostriker 2007; Zinnecker & Yorke 2007). High density is one of the essential conditions for molecular clouds to collapse. There are many mechanisms that can compress gas to achieve high density condition, such as transporting material through filament accretion (Peretto et al. 2013; Motte et al. 2015, 2017), compressing gas through stellar feedback (such as supernova feedback (Herbst & Assousa 1978), massive star ionized hydrogen feedback (Whitworth et al. 1994), etc.) and dynamic feedback (such as cloud-cloud collision process (Habe & Ohta 1992)). All of these mechanisms can explain the formation of dense regions in galaxies, which are hotbeds for star formation.

Massive star formation has attracted much attention in the past

few decades because it plays an important role in galaxy formation and evolution (McKee & Tan 2003). However, the mechanism of which is a long-standing problem. The difficulty of massive star formation lies in achieving their initial conditions (ultra-high density) and balancing their strong feedback (radiation pressure greater than gravitational potential). The cloud-cloud collision (CCC) process works well to address the ultra-high density conditions (Takahira et al. 2018). Collisions between two or more molecular clouds can produce supersonic shock waves in collisional area, which can greatly compress gas, allowing large amounts of matter to be concentrated in small-scale structures for a short period of time (typical compression timescale of 0.1 ~ 0.5 Myr), and eventually collapse to form massive stars. Star formation triggered by dynamic feedback can effectively regulate the star formation rate of galaxies, such as the formation of super star clusters (SSC) or mini-starbursts in the local region of galaxies (Fukui et al. 2021), where the contribution of cloud-cloud collision cannot be ignored. Cloud-cloud collision process occur very frequently in galaxies (Tasker & Tan 2009), and 10% (up to half) of the galaxy's total star formation are caused by such process (Kobayashi et al. 2018).

A pioneering simulation work of CCC was performed by Habe & Ohta (1992), in which a basic scenario of CCC was presented. They advanced that a dense gas layer can be facilitated by the compression from supersonic collision, and it induce the formation of dense self-

* E-mail: chenen@pmo.ac.cn

gravitating clumps which may finally evolve into clusters containing high-mass stars. CCC is an effective trigger of massive, dense cores formation. In the recent hydrodynamical simulations (e.g., Takahira et al. 2014; Takahira et al. 2018), a bulk of cores are born in the shocked regions and the number and mass of cores are controlled by the relative collision speeds (typically at 10 km s^{-1}). A larger relative speed could increase the number of cores, but on the contrary, it suppresses the mass growth of cores due to short collision timescale for cores to accrete gas. Therefore, collisions of two clouds with different initial conditions (such as size, mass and collision speeds) may result in a wide range of stellar mass, for example, a single or several O stars triggered by smaller molecular clouds ($M > 10^{3-5} M_{\odot}$) collisions, including L1188 (Gong et al. 2017), N159W-S in LMC (Fukui et al. 2015), Trifid Nebula M20 (Torii et al. 2011, 2017b), RCW 120 (Torii et al. 2015), S235 (Dewangan et al. 2017), Sh2-48 (Torii et al. 2017a), and RCW 34 (Hayashi et al. 2018); a Super Star Cluster (SSC) or a mini-starburst triggered by massive molecular cloud ($M > 10^{5-6} M_{\odot}$), including Westerlund 2 (Furukawa et al. 2009), NGC3603 (Fukui et al. 2014), RCW38 (Fukui et al. 2016), W51A (Fujita et al. 2017), and NGC6334/NGC6357 (Fukui et al. 2018).

Among these observations, the 'bridge feature' shown in position-velocity diagrams was believed to be the commonest signature of CCC. The bridge feature is the coherent gas which connects the two colliding clouds and the turbulent motion inside would be enhanced by collisions (Wu et al. 2017). This feature can also be reproduced by the numerical simulations calculated by Anathpindika (2010) and Takahira et al. (2014). Other observational signatures such as the complementary spatial distribution of adjacent clouds and the cavity created on the larger cloud are also very important evidences to prove a collision event. However these signatures could not always be seen in a particular collision event due to the variant collision stages and different projection along the line-of-sight. Fukui et al. (2018) summarized previous studies and listed the main observational signatures of CCC as: a) the supersonic velocity separation of the colliding clouds, b) the complementary distribution of them, and c) the bridge feature connecting clouds. These signatures are useful guidance to search more collision candidates in spectroscopic observations.

The S235 complex, known as an active star-forming complex, is part of the giant molecular cloud G174+2.5 in the Perseus Spiral Arm (Heyer et al. 1996) toward the anti-Galactic Plane ($l, b \sim (173^{\circ}.6, 2^{\circ}.8)$). Figure 1 shows the color-composite images of the S235 region that was obtained by *Spitzer* IRAC 3.6 μm (blue) and 8 μm (green), and *Spitzer* MIPS 24 μm (red) images. The molecular complex mainly hosts the S235 HII region (the yellow ring) with a diameter of $\sim 3 \text{ pc}$ and a slight faint cloud with three ultra-compact (UC) HII regions (S235-A, S235-B and S235-C) on it in the south. The S235 HII region who was excited by a single O9.5V type star BD+35 $^{\circ}$ 1201 (Georgelin et al. 1973), was surrounded by a dust ring with an opening end toward the south. The distance of S235 was estimated to be 1.8 kpc by Evans & Blair (1981). S235 is a very well studied site using multi-wavelength datasets spanning from near-infrared (NIR) to radio wavelengths. Over a hundred of young stellar objects (YSOs) were found in the extended S235 region (e.g., Dewangan & Anandarao 2011; Dewangan et al. 2016) and totally nine young embedded clusters (ECs) were identified in some well known star forming sites called East 1, East 2, North-West, Central and S235A, S235B and S235C, suggesting a sequential star formation in the molecular complex (Camargo et al. 2011).

In the early studies, Evans & Blair (1981) found two main velocity components (-20 km s^{-1} and -17 km s^{-1}) toward the S235 region.

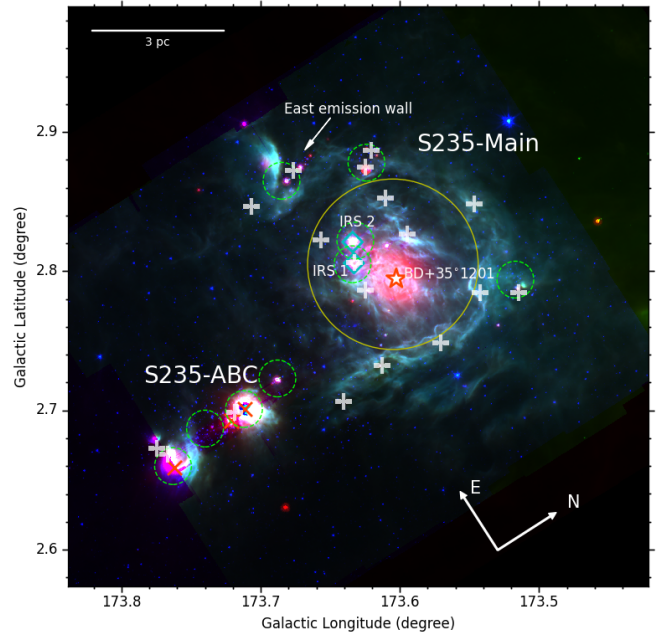


Figure 1. Color composite image of the S235 complex. Blue, green and red show the *Spitzer* IRAC 3.6 μm , 8 μm and *Spitzer* MIPS 24 μm , respectively. The complex mainly hosts two molecular clouds, the S235-Main and the S235-ABC. The red asterisk symbol indicates the exciting O star BD+35 $^{\circ}$ 1201 of the S235 HII region (the yellow ring) and the red crosses indicate B type stars in S235-ABC. The cyan diamonds indicate the two bright infrared sources IRS 1 and IRS 2. The green dashed circles indicate the position of nine young star clusters. The white pluses indicate the Bolocam clumps at 1.1 mm. A nebular emission is designated as eastern emission wall which is far away from the exciting O star.

We hereafter refer to the -20 km s^{-1} cloud as the "S235-Main" and the -17 km s^{-1} cloud as the "S235-ABC". The S235-Main cloud was associated with an evolved HII region (S235 HII region) with a nearly sphere-like shell (a diameter of $\sim 3 \text{ pc}$), harboring at least four star forming sites (i.e., East 1, East 2, North-West, and Central). Furthermore, the S235-Main was constructed by three gas components in details (i.e., $-18 \sim -15 \text{ km s}^{-1}$ (red), $-21 \sim -18 \text{ km s}^{-1}$ (central), and $-25 \sim -21 \text{ km s}^{-1}$ (blue)) traced by $^{13}\text{CO} (1-0)$ line data (Kirsanova et al. 2008), which shows a C-like structure in position-velocity diagram, indicating an expanding motion of the S235 HII region (Dewangan et al. 2016). The spatial distribution of the star forming sites and the kinematics of molecular gas in the S235-Main cloud suggest that the expansion of the S235 HII region could be responsible for the star formation around the shell. On the other hand, the S235-ABC cloud only harbors three star forming sites (i.e., S235 A, S235 B and S235 C), embedding with three B type stars respectively. The sites of these stars are located at about 5–6 pc south of the S235-Main which is larger than the diameter of the S235 HII region, suggesting that their star formation could not be triggered by the expansion of the S235 HII region ionization front (Camargo et al. 2011). However, several observational signatures such as broad bridge feature in velocity phase and complementary molecular pair of S235-Main and S235-ABC were found by Dewangan & Ojha (2017) using FCRAO $^{12}\text{CO} (1-0)$ and $^{13}\text{CO} (1-0)$ datasets suggesting that the two clouds were suffering the CCC process. Their analysis revealed that the CCC process might have influenced the star formation activity along the colliding inter-

face (i.e., East 1 and S235-ABC), which triggered the formation of massive stars and young stellar clusters in S235.

Although the CCC signatures are significant toward the S235 region, the connection between the CCC process and the star formation activity, especially its effects on triggering star formation in the two colliding clouds has not been studied. In this paper we present the results of our new observations of ^{12}CO (1–0), ^{13}CO (1–0) and C^{18}O (1–0) with angular resolutions of $52''$ (at 115 GHz) to $55''$ (at 110 GHz) using the PMO-13.7m telescope. The data was also combined with other archived data such as parallax observations from the Gaia satellite (Gaia Collaboration et al. 2016), NIR data from the UKIDSS Galactic Plane Survey (UKIDSS-GPS; Lawrence et al. 2007), NIR and MIR data from *Spitzer*, dust continuum 1.1 mm data from the Bolocam Galactic Plane Survey (BGPS; Aguirre et al. 2011), and radio continuum data from the Canadian Galactic Plane Survey (CGPS; English et al. 1998) to investigate the detailed scenario of CCC in S235 and its effects on triggering star/core formation. Section 2 describes the observations and data reductions and Section 3 presents the observation results. Discussions are given in Section 3.5 and conclusions are placed in Section 4.

2 OBSERVATIONS

2.1 PMO-13.7m CO observations

We employed the PMO-13.7m single-dish sub-millimeter telescope to study the distributions and kinematics of the molecular material associated with the S235 complex. The observations of S235 were made as part of the Milky Way Imaging Scroll Painting (MWISP¹) project which is aimed at mapping the large-scale molecular gas with CO and its isotope molecular lines along the northern Galactic Plane. The project is conducted by the PMO-13.7m telescope, which is located at Delingha (3200m altitude), Qinghai, China. This antenna can observe three CO molecular lines, ^{12}CO (1–0), ^{13}CO (1–0), and C^{18}O (1–0) simultaneously. The 3×3-beam Superconducting Spectroscopic Array Receiver (SSAR) system is used as front end, which provides a 1 GHz bandwidth with 16384 channels and a spectral resolution of 61 kHz, equivalent to a velocity coverage of $\sim 2600 \text{ km s}^{-1}$ and a velocity resolution of $\sim 0.17 \text{ km s}^{-1}$ at 110 GHz. The detailed properties of this system are described in Shan et al. (2012). In order to observe the three low-J CO lines simultaneously, the ^{12}CO (1–0) line was set at the center of the upper sideband so that the lower sideband is able to cover both ^{13}CO (1–0) and C^{18}O (1–0) lines. Observations were undertaken in position-switch on-the-fly (OTF) mapping mode. The observed region was divided into several $30' \times 30'$ cells and each cell was scanned at least in two orthogonal directions, along the galactic longitude and the galactic latitude, to reduce scanning effects.

According to the status report² of the PMO-13.7m telescope, the beam efficiency B_{eff} , which is used to convert the antenna temperature (T_A) to the main beam temperature with the relation $T_{mb} = T_A/B_{eff}$, can reach to 46% at 115 GHz and 49% at 110GHz. The receiver equipped with on the telescope provides typical system temperatures of 191–381 K at the upper sideband, and 142–237 K at the lower sideband. Therefore, the typical rms noise level is about 0.5 K (T_{mb}) for ^{12}CO (1–0), and 0.3 K (T_{mb}) for ^{13}CO (1–0) and C^{18}O (1–0) at a channel width of $\sim 0.17 \text{ km s}^{-1}$. The telescope has a

beam size of $55''$ at 110 GHz and $52''$ at 115 GHz, and the pointing of the telescope has an rms accuracy of about $5''$.

Data reduction was done with CLASS and GreG in the software GILDAS³. The final data product was convert into fits file format with pixel size of $30'' \times 30''$. A field of $25' \times 25'$ centred at $(l, b) \sim (173^\circ.625, 2^\circ.790)$ is taken in this work. Throughout this paper, the galactic coordinate system is utilized and the equinox is J2000.0, and velocities are all given with respect to the local standard of rest (LSR).

2.2 Archival data

We obtained the near-infrared (NIR) J, H, K band point sources catalog from the UKIDSS-GPS data release (Lawrence et al. 2007) and the selection procedures of the UKIDSS-GPS photometry were following Dewangan et al. (2015). Only brighter NIR sources ($H < 12.3$ and $K < 11.4$ mag) were extracted from 2MASS (Skrutskie et al. 2006) to take the place of the sources from UKIDSS-GPS in order to avoid saturation. Using the NIR data in combination with the *Spitzer* MIR data (Fazio et al. 2004), we searched for the disk-bearing young stellar object (YSO) candidates in the surveyed region (details are described in Section 3.4.1). We made use of the Bolocam Galactic Plane Survey (BGPS) of 1.1 mm dust continuum emission (Rosolowsky et al. 2010; Aguirre et al. 2011; Ginsburg et al. 2013) and the available nightly observations of James Clerk Maxwell Telescope (JCMT) Submillimeter Common-User Bolometer Array 2 (SCUBA-2; Dempsey et al. 2013; Chapin et al. 2013) of $850 \mu\text{m}$ emission (Project ID: MJLSY02) to study the dust clumps and cores (more details are described in Section 3.3). The angular resolution of the 1.1 mm map is $\sim 33''$ while the $850 \mu\text{m}$ map has a higher resolution of $\sim 14''$. The 1420 MHz radio continuum data were obtained from the Canadian Galactic Plane Survey (CGPS; English et al. 1998) with beam size of $\sim 1'$. In order to calibrate the distance of the S235 molecular cloud, we also utilized the parallax data from Gaia data release 3 (Gaia Collaboration et al. 2021).

3 RESULTS AND DISCUSSIONS

3.1 Molecular gas distributions with PMO-13.7m

We obtained ^{12}CO ($J=1-0$), ^{13}CO ($J=1-0$) and C^{18}O ($J=1-0$) line emissions simultaneously by PMO-13.7m telescope. Two major molecular clouds, namely the S235-Main and the S235-ABC, were revealed base on the gas kinetics motion. Our CO data has a similar spatial resolution with the FCARO CO data. With the CO data, we can reproduce the results of cloud-cloud collision in S235 which has been presented in Dewangan & Ojha (2017). Our data has better velocity resolution (0.17 km s^{-1}) than FCRAO data (0.266 km s^{-1}), which can reveal more detailed velocity components, such as bridge features with coherent gas. Additional observation of C^{18}O ($J=1-0$) could reveal more clumpy regions associated with dense regions (or star formation regions).

Figure 2 show the position-velocity (PV) diagrams of ^{12}CO (background) and ^{13}CO (contours) toward the survey region. The S235-Main is the blue-shifted cloud with a velocity range from -24 to -18.5 km s^{-1} and a mean velocity of -20.5 km s^{-1} , while the S235-ABC is the red-shifted cloud with a velocity range from -18.5 to -13.5 km s^{-1} and a mean velocity of -16.5 km s^{-1} . Therefore, there is $\sim 4 \text{ km s}^{-1}$ velocity separation between the two clouds along

¹ <http://www.radioast.nsd.cnmwisp.php/>

² <http://english.dlh.pmo.cas.cn/fs/>

³ <https://www.iram.fr/IRAMFR/GILDAS/>

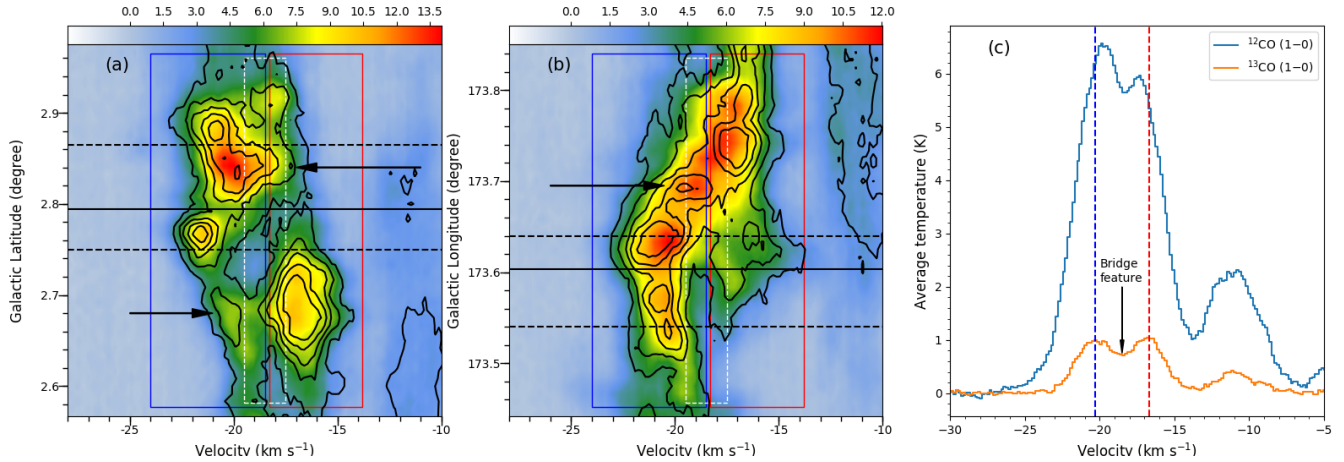


Figure 2. Position-velocity diagrams of the S235 complex. Contours in (a) and (b) show the averaged intensity of the PMO-13.7m ^{13}CO (1-0) data while the background color image shows that of the ^{12}CO (1-0) data. The horizontal black solid line and dashed lines indicate the position of the exciting O star and the approximate extension of the $8\ \mu\text{m}$ ring, respectively. The blue and red rectangle highlight the velocity range of the S235-Main cloud ($-24 \sim -18.5\ \text{km s}^{-1}$) and the S235-ABC cloud ($-18.5 \sim -13.5\ \text{km s}^{-1}$), respectively, while the white dashed rectangle highlights the intermediate velocity range ($-19.5 \sim -17.5\ \text{km s}^{-1}$) of the bridge feature which was significantly influenced by collision. (c) shows the average spectrum of the whole region. The black arrows in all panels represent the bridge feature that connects the two separated clouds.

light-of-sight. Note that the two clouds are not completely separated, they are connected to each other by bridge feature (black arrows in Figure 2), which has a velocity range of -19.5 to $-17.5\ \text{km s}^{-1}$. The bridge feature is the compressed gas layer decelerated by the collision, which transforms the kinetic motion of the molecular cloud into a turbulent motion with a broad velocity dispersion. The existence of a broad bridge feature in velocity space indicates an observational signature of collisions between molecular clouds Torii et al. (2017b).

On the other hand, we can also see a semi-ring-like or C-like structure in the blue-shifted velocity phase. As shown in Figure 2a&b, the horizontal black solid line and the dashed lines indicate the position of the exciting O star of the S235 HII region and the approximate extent of the $8\ \mu\text{m}$ ring emission, respectively. This structure is a signature of an expanding shell of the HII region, which is in agreement with the previous work of Dewangan et al. (2016), which detected an expansion velocity of the gas to be $\sim 3\ \text{km s}^{-1}$. Therefore the S235-Main was mainly shaped by the S235 HII region, while the S235-ABC may not be affected by the expansion shock of the S235 HII region due to the larger separation velocity of $4\ \text{km s}^{-1}$.

The observational signatures of cloud-cloud collision in S235 has been discussed in the work of Dewangan & Ojha (2017). They used the first and the second momentum maps of ^{12}CO and ^{13}CO to trace the boundary and colliding interface of the two clouds. As shown in Figure 3a–c, we reproduced the momentum maps for the ^{13}CO ($J=1-0$) emission using our PMO-13.7m data. A distinct boundary between the S235-Main and the S235-ABC is found in the first momentum map (moment 1). The convex distribution in the north of S235-ABC just matches the concave distribution in the south of S235-Main. This perfect complementary distribution (concave-convex pairs) indicates that the S235-Main may have physical connection with the S235-ABC. Moreover, as shown in the second momentum map (moment 2), the boundary region has a velocity dispersion of $\sim 2\ \text{km s}^{-1}$ which nearly double the velocity dispersion of each cloud. This large velocity dispersion can be interpreted as the overlap or interaction of the two clouds in the line-of-sight. If two clouds are at the same distance, then there is an interaction between them, such as cloud-cloud collision. We will measure the distance of each cloud in Section 3.2

to support this point. Therefore, a possible colliding interface (highlighted by the purple dashed line) can be found in the boundary of the two clouds. We also checked the position-velocity (PV) distribution along the colliding interface by five PV-cuts (A to F) in Figure 3d–f. PV-cuts from A to C show a broad single velocity component with an average velocity of $\sim -18\ \text{km s}^{-1}$, which represents the intermediate velocity bridge feature that connects the S235-Main and the S235-ABC, indicating that the two clouds may have been interacted with each other and converted their dynamical motion into the turbulent motion. However, PV-cuts from C to F clearly show two velocity components that refer to the S235-Main and the S235-ABC velocity domain respectively, indicating that the two clouds may overlay in these regions in the line-of-sight or may be colliding or separating with each other in the near future. The averaged CO spectrum of the interface is shown in Figure 3f, which presents a bridge feature of flattened profile in the intermediate velocity range.

In conclusion, the supersonic velocity separation ($\sim 4\ \text{km s}^{-1}$), the spatial complementary distribution of the molecular cloud pairs and the broad velocity bridge feature along the colliding interface are distinct signatures of cloud-cloud collision process between the S235-Main and the S235-ABC, which is consistent with the results of Dewangan & Ojha (2017). Detail distance measurement of the two clouds will support this point.

3.2 Molecular cloud identification and distance measurement

The distance of S235 is commonly used as 1.8 kpc in literature (e.g., Evans & Blair 1981), but this value is not particularly strict. It was estimated based on the intermediate value of earlier studies such as the 2.1 kpc distance from the O-star determined by Georgelin et al. (1973) and the 1.6 kpc distance from the nebula estimated by Kazes et al. (1977). We employed a method based on Gaia DR2 parallax and G-band extinction (A_G) measurement introduced by Yan et al. (2019b) to measure the distance of each velocity component in S235. This method made use of the boundary of molecular clouds and the estimation of parallax as well as the extinction of stars by Gaia satellite.

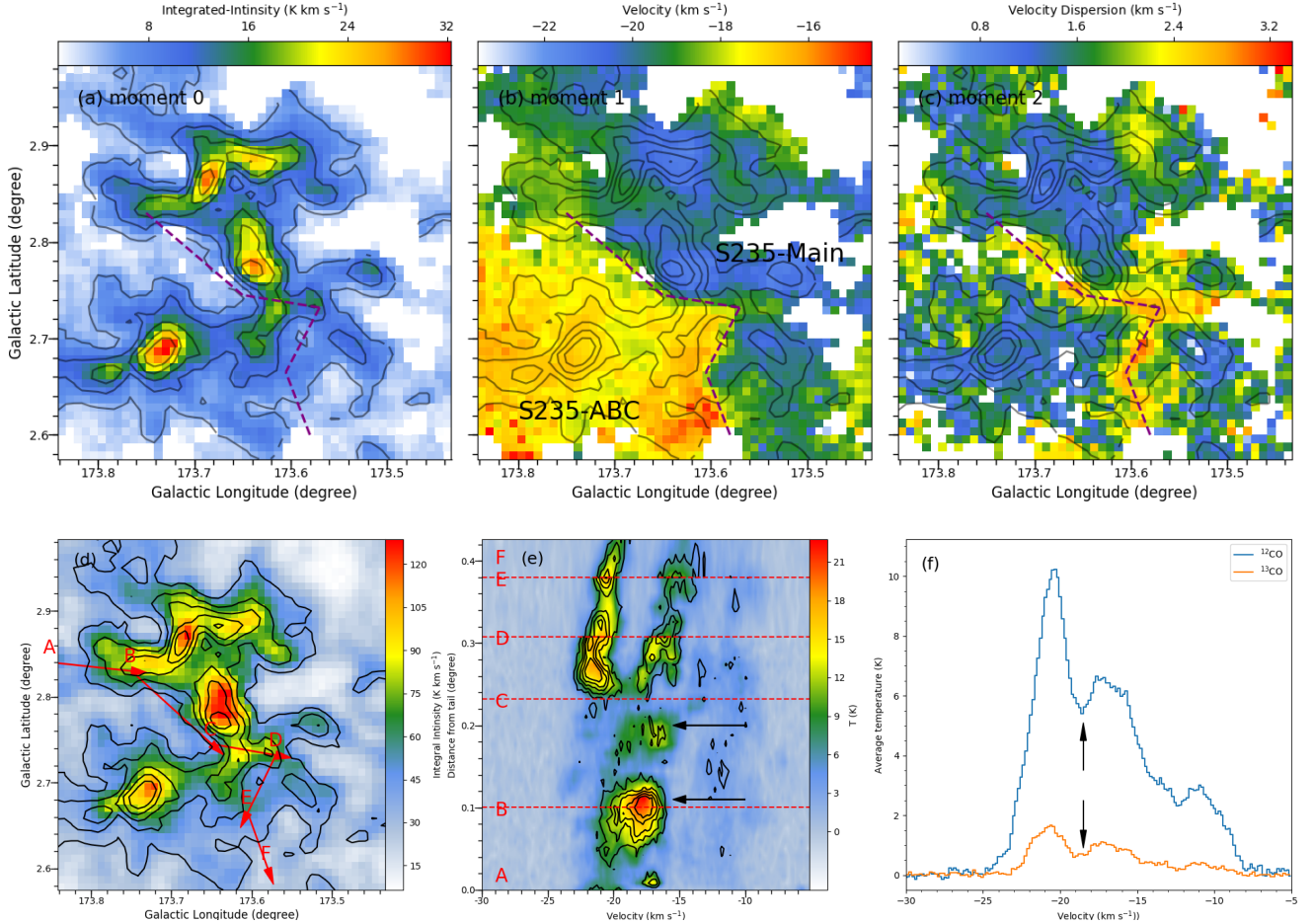


Figure 3. (a)–(c) ^{13}CO momentum maps of the S235 complex. The integrated velocity ranges from -24 km s^{-1} to -13.5 km s^{-1} . Pixels where the maximum intensity value within that velocity range less than 0.9 K (3σ noise) are omitted and set to blank. The moment 0, moment 1 and moment 2 maps are presented in the left, center and right respectively. The contours represent the integrated intensity of the ^{13}CO whose intensity levels start from 5 K km s^{-1} (5.5σ) to 30 K km s^{-1} with steps of 5 K km s^{-1} . The purple dashed line highlights the possible collision interface between S235-Main and S235-ABC. (d) Five position-velocity cuts (PV-cuts) along the interface with markers A-F. (e) Position-velocity diagram of the PV-cuts. (f) Average spectrum along the interface. The black arrows in all panels depicted the bridge feature.

In the method, the first step is to identify the boundary of each molecular cloud by decomposing the ^{13}CO lines into individual components with Gaussian fitting. Due to the spatial consistency of the molecular cloud, the pixel points with similar line-center velocity, similar spectral line broadening and intensity are clustered, so as to identify each cloud. In this work, we use ACORNS⁴ (Agglomerative Clustering for ORganising Nested Structures) clustering to distinguish clouds (Henshaw et al. 2019). ACORNS is a clustering tool based on a technique known as hierarchical agglomerative clustering, whose primary function is to generate a hierarchical clustering system in discrete data.

In the clustering results, each Tree corresponds to a cloud. For a Tree with hierarchical structure, the cloud is a complex composed of discrete sub-structures without overlapping in the projection phase. On the other hand, for a Tree without hierarchical structure, the cloud is a relatively uniform and coherent structure. The positions of the outermost pixels are connected to form the boundary of the cloud on

the projection plane. In the line-of-sight direction, the Gaussian fitting line width of the corresponding position is taken as the thickness of the cloud. Consistent with this, the range of the line-center velocity within $\pm 3\sigma$ is taken as the velocity range of the cloud. Therefore, according to the clustering method mentioned above, the velocities of adjacent pixels are similar, which makes the cloud have a relatively smooth contour in the PPV space.

For the next step, we divide Gaia stars into two classes, i.e. on-cloud stars and off-cloud stars, according to the boundary of individual molecular cloud. Due to the high extinction across molecular clouds, the starlight will be attenuated when passing through the molecular cloud, so that the extinction value will significantly change between the foreground and background of the molecular cloud. Therefore, the parallax of the extinction jump point represents the true distance of the molecular cloud.

The final step is to build a Bayesian model to estimate the distance to the on-cloud stars, and solve the parameters in the model with Markov chain Monte Carlo (MCMC) sampling. The position of jump point (D), the extinction value of foreground and background (A_G) and its standard deviation (σ) were selected as priors, and the

⁴ <https://github.com/jdhenshaw/acorns>.

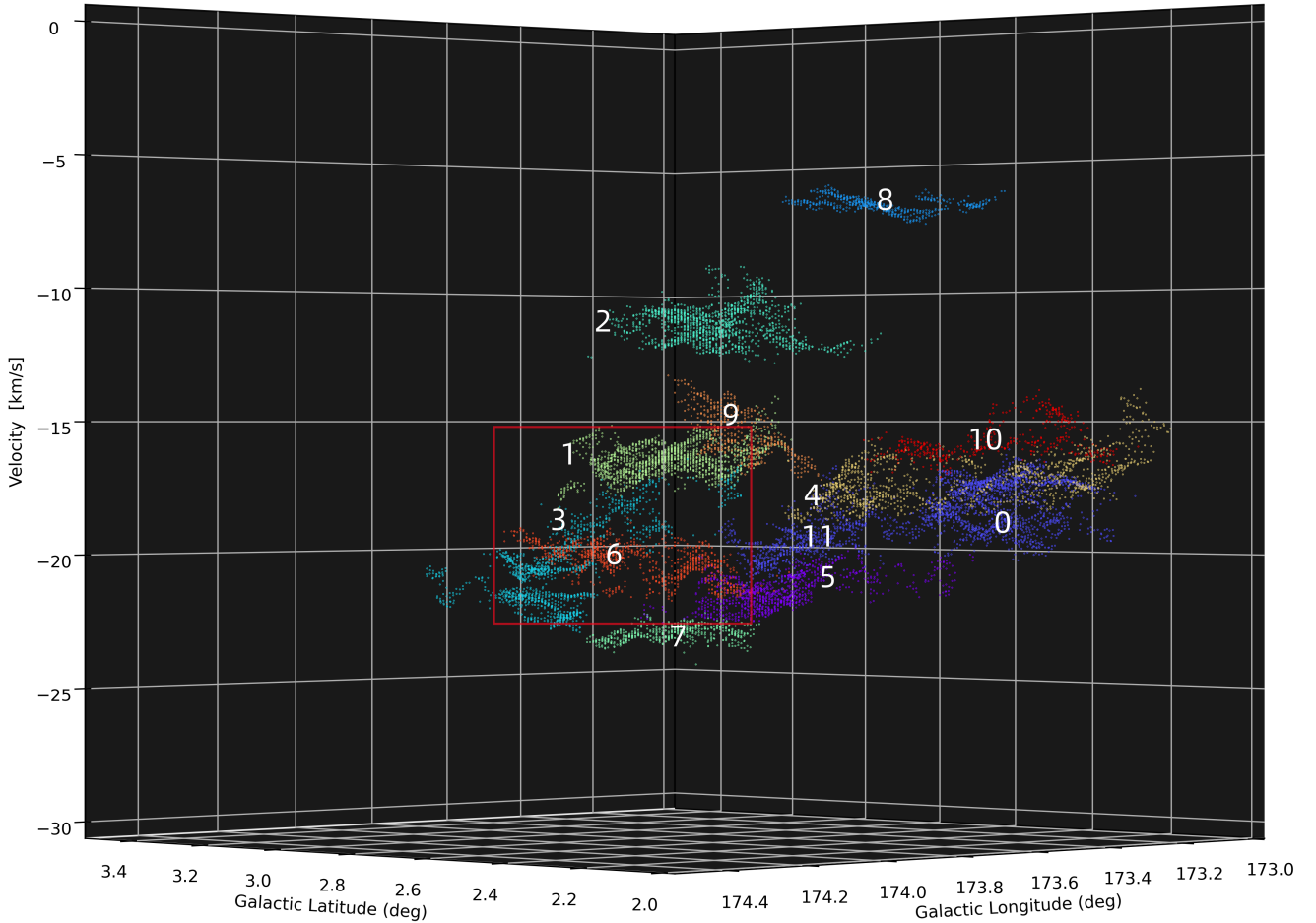


Figure 4. Three-dimensional presentation of molecular cloud clustering decomposition in the extended S235 region. The red box represents the extent of the S235 study area, which contains three components marked with label 1, 3 and 6.

truncated Gaussian model was used as the probability density distribution. Considering that most of the distance of this area is within 3 kpc, and the extinction is very strong, we set the distance of the jump point to be evenly distributed from 100 to 3000 pc. The initial distance value is set to the average distance of the selected stars. Both the extinction value and its deviation are set as exponential distribution. The selection of initial value and the combination of errors follow the method from [Yan et al. \(2019a\)](#).

Figure 4 shows the 3D PPV molecular cloud clustering of the extended S235 area ($173^{\circ}.0 < l < 174^{\circ}.5$, $2^{\circ} < b < 3^{\circ}.5$). A total of 12 cloud components are decomposed in this region, among which the red box region is the main molecular cloud components in the S235 study area in the paper, including molecular clouds marked with label 1, 3 and 6 in the figure, which correspond to cloud-3, cloud-2 and cloud-1 in the latter part of the paper respectively. The properties of these three molecular components are listed in table 1.

The boundary of the cloud on the projection plane is used as the selection standard for on-cloud stars. For the reference area used for extinction background deduction, we use the integral intensity map of ^{12}CO emission to select stars in an area with no or very weak ^{12}CO emission. If the boundary of the cloud is indeed coherent in three

dimensions and at a determinate distance, then all the stars within the boundary can result to the jump caused by the extinction of the cloud to the greatest extent. Different clouds, on the other hand, are likely to be located at different distances. According to the fitting results, for ^{13}CO , most pixels have only one component on the spectral line, that is, there is no overlap between clouds at this position. Therefore, for a cloud with relatively large angular scale can be basically determined that the jump in star extinction is from this block structure. However, for most clouds, the overlap of light-of-sight direction is inevitable. We can analyze the measurement results as follows:

If two large cloud with partially overlap in the line-of-sight, firstly, in the non-overlapping part, we directly measure the distance of this part according to the extinction jump within the cloud boundary. However, in the overlapping part, we don't know yet how many stars are in front of, behind or between the two clouds. When we add these stars into our calculations, if the measured distances don't change much, then the stars are in front or behind the structure, which also means that the two clouds lay very close. On the other hand, if the measurement change significantly, such as showing multiple extinction jumps, then the respective distances between this component and its neighboring velocity component can be inferred by comparison. For example, we

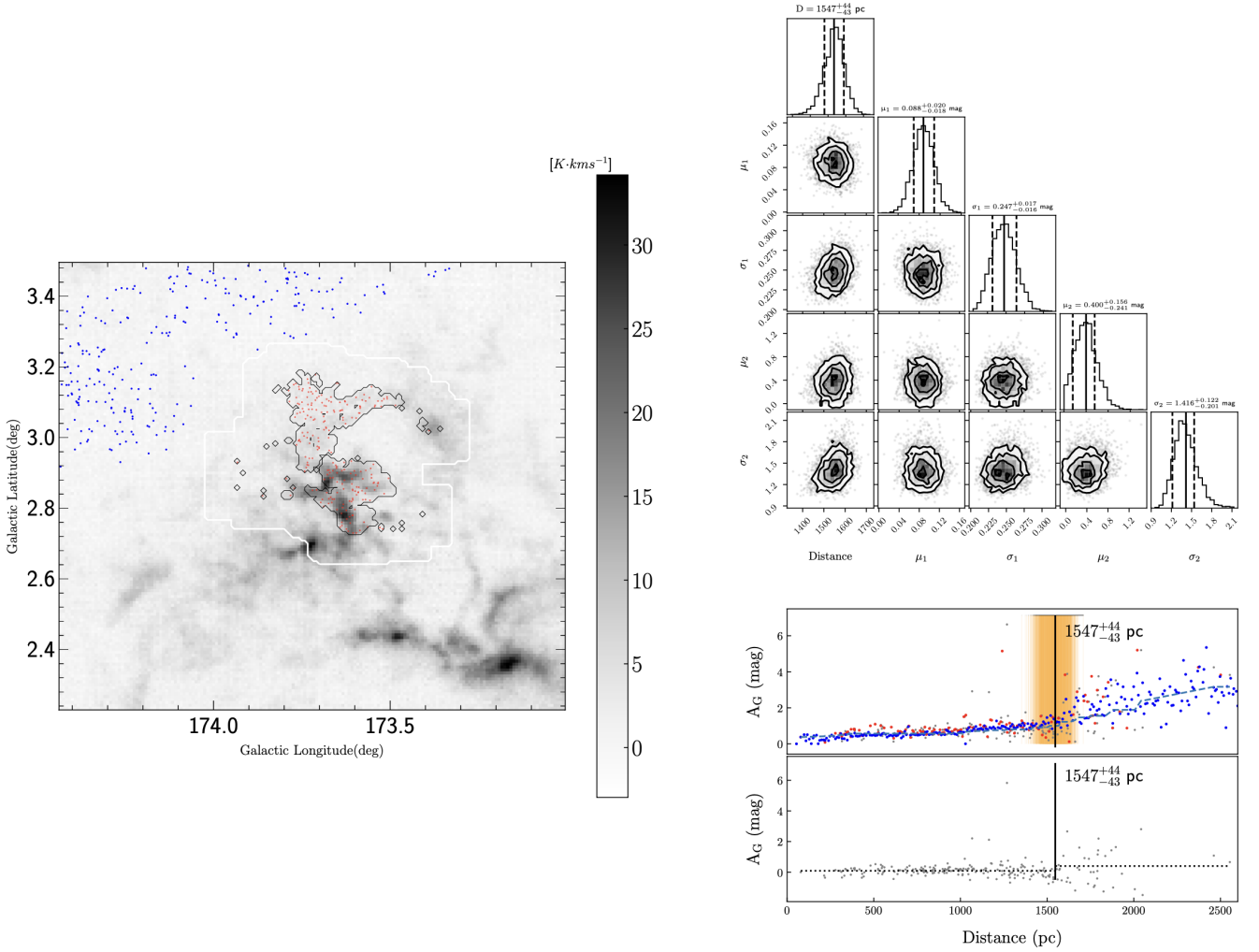


Figure 5. Distance measurement of the molecular cloud component cloud-1 in the S235 region. The gray scale on the left panel shows the ^{13}CO integral intensity map for the selected data area. Black contour is the boundary of the velocity component ^{13}CO molecular cloud found by cloud segmentation algorithm. White contour is the extension of the molecular cloud boundary contour. The red dots represent the position of on-cloud stars, while the blue dots represent the stars in the selected reference region, which exclude the region with obvious ^{12}CO emission and the region within the white contour to reduce the effect of background extinction on the background subtraction. The upper right panel is the corner plot of MCMC sampling. The upper and lower subgraphs in the lower right panel respectively represent the A_G -Distance diagram before and after the baseline of background extinction fitting is subtracted. The data used for MCMC fitting is the data after baseline subtraction. The black vertical line represents the median distance obtained by sampling, the orange translucent thin line represents all the posterior sampling results, and the confidence interval with the upper and lower indices of the distance is 1σ . The error here is a mathematical statistical error and the actual error should be plus a systematic error of about 5%.

can firstly determine the distance of one cloud who has the maximum number of on-cloud stars. And then we can infer the distance of the other clouds by comparing to the relative extinction jumps.

According to the methods mentioned above, molecular clouds in the S235 region were decomposed into three components, and the distance parameters of each component were determined by the position of extinction jump. The measurement results were shown in Figure 5, Figure 6 and Figure 7 for component cloud-1, cloud-2 and cloud-3, respectively. And their physical properties are listed in table 1.

These three molecular cloud components basically cover the S235 region, as well as the aforementioned velocity extent. The cloud-1 has a central velocity of -20.4 km s^{-1} , corresponding to a blue-shifted cloud associated with the S235-Main, while the cloud-3 has a central velocity of -16.5 km s^{-1} , corresponding to a red-shifted

cloud associated with the S235-ABC. Moreover, the cloud-2 with the central velocity of -19.8 km s^{-1} corresponds to the bridge feature of the intermediate velocity, who connects the cloud-1 and the cloud-3. Furthermore, the distances of these three molecular clouds are basically the same within 1σ error range according to the distance measurement results, in which the cloud-1 is $1547^{+44}_{-43}\text{ pc}$, the cloud-2 is $1543^{+35}_{-30}\text{ pc}$, and the cloud-3 is $1567^{+33}_{-39}\text{ pc}$, indicating that the cloud-1 and cloud-3 are likely to collide with each other at the same place, while the cloud-2 is the coherence bridge feature connecting the two clouds.

Based on the distances of these three clouds, we calculate the mean distance of the S235 molecular cloud complex to be 1552 pc , which is nearly 250 pc different from the 1.8 kpc given in literature (e.g., Evans & Blair 1981; Dewangan & Ojha 2017), but close to the result

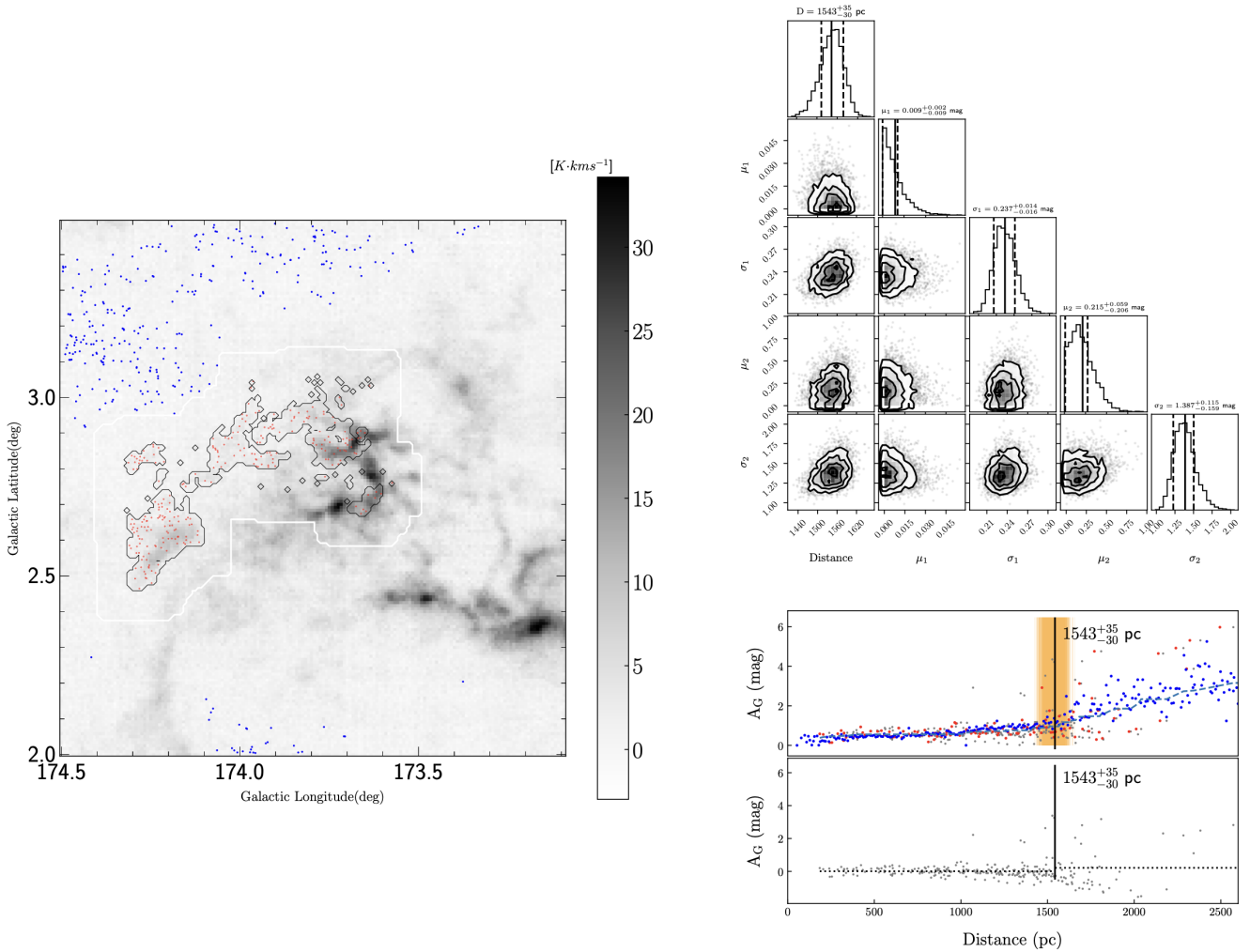


Figure 6. Distance measurement of molecular cloud component cloud-2 in S235 region, and mapping method is consistent with Figure 5.

Table 1. Properties of molecular cloud components of S235.

cloud id	l_{cen} deg	b_{cen} deg	v_{cen} km s ⁻¹	Δv km s ⁻¹	Area arcmin ²	Flux K km s ⁻¹	\bar{N} cm ⁻²	D pc	foreAg mag	backAg mag
cloud-1	173.642	2.910	-20.4	1.2	226.5	5144.5	5.5E+21	1547 ⁺⁴⁴ ₋₄₃	0.09±0.25	0.408±1.43
cloud-2	173.937	2.773	-19.8	1.8	310	4599.5	3.0E+21	1543 ⁺³⁵ ₋₃₀	0.009±0.237	0.215±1.387
cloud-3	173.801	2.671	-16.5	1	346.5	6677.9	4.1E+21	1567 ⁺³³ ₋₃₉	0.018±0.316	0.704±1.78

of Kazes et al. (1977) of 1.6 kpc. Since our distance measurement is based on the parallax measurement method of Gaia satellite with higher accuracy, the distance of S235 is set as 1552 pc or 1.55 kpc hereafter in the paper.

3.3 Clumps and cores

Clumps and cores are fundamental units of star formation (e.g., Bergin & Tafalla 2007). We searched for ¹³CO clumps because ¹³CO (J= 1 – 0) is optical thin ($\tau \approx 0.1 \sim 0.9$ with an average of 0.355, less than 1) thus can retain the properties of total molecular gas. We also checked the C¹⁸O emission for each ¹³CO clumps in as much as it can trace higher density gas due to its lower abundance.

On the other hand, we also identified the SCUBA-2 850 μ m dust cores in the survey region relying on its higher sensitivity and small beam size (HPBW= 14'', 1/4 of PMO-13.7m). All the clumps and cores are obtained with *dendrograms*⁵ algorithm, which is able to extract hierarchical substructures of the dataset (2-D image or 3-D cube) into a set of iso-surfaces to form the skeleton with leaves or branches of the family tree. The top levels named 'leaves' of the tree are the most dense substructures of the dataset with a single local maximum, while the bottom levels named 'trunks' represent the low density extended structures.

⁵ <http://www.dendrograms.org/>

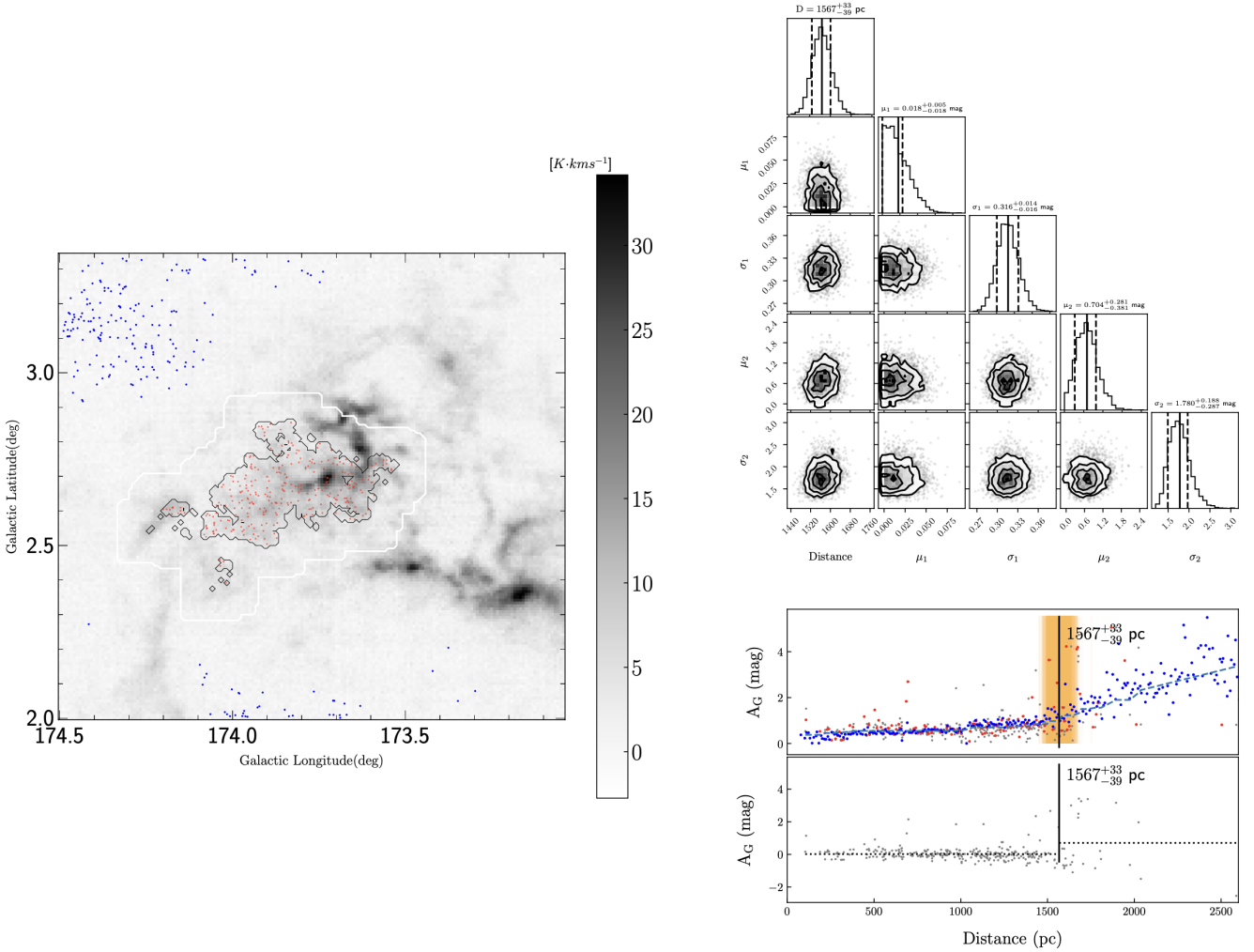


Figure 7. Distance measurement of molecular cloud component cloud-3 in S235 region, and mapping method is consistent with Figure 5.

We performed 3-D (Position-Position-Velocity, PPV) dendrograms for ^{13}CO and C^{18}O data cube. As for ^{13}CO cube, we obtained clumps based on a minimum detection level of $2\sigma_{rms}$ ($1\sigma_{rms} \sim 0.3\text{ K}$) and then identified branches and leaves from their parent structures with the parameters of the minimum increment of $2\sigma_{rms}$ and the minimum number of pixels of 54 (3×3 pixels \times 6 velocity channels, corresponding to 1.6 beam size). We also set a high threshold of $15\sigma_{rms}$ in order to obtain the densest structures and exclude the extended ones. In the paper, the data of C^{18}O is from the Milky Way Imaging Scroll Painting (MWISP) with rms level of about 0.3 K, which is not sensitive enough to detect the relative fainter C^{18}O clumps. In order to obtain them, we use a detection limit of $2\sigma_{rms}$. The minimum increment is also set to $2\sigma_{rms}$, and the same iso-surface pixel number of 54 is set. As a result, ten ^{13}CO clumps were extracted by dendrograms and eight of them with C^{18}O clump counterparts. The physical properties of the ^{13}CO clumps and the C^{18}O clumps are listed in Table 2 and Table 3 respectively. Note that the poor emission of the C^{18}O may caused large uncertainties on mass estimation.

The radius of the clumps were computed from the geometric mean of the intensity weighted second moments along the major and minor axis. And the mass of clumps were calculated from the standard

LTE methods. We estimated the excitation temperature from the peak brightness temperature of ^{12}CO due to its optically thick, and calculated the opacities, column densities and LTE masses of the clumps by accepting a constant $[\text{H}_2/^{12}\text{CO}]$ abundance ratio of 1.1×10^4 (Frerking et al. 1982) and isotopic ratio $[\text{C}^{16}/\text{C}^{18}] = 560$ (Wilson & Rood 1994), and $[\text{C}^{12}/\text{C}^{13}] = 6.21d_{GC} + 18.7$ which flows a gradient relation along the distance from the galactic center (Milam et al. 2005). At the distance $D = 1.55\text{ kpc}$ towards anti-galactic center, d_{GC} of S235 is about 10.25 kpc thus $[\text{C}^{12}/\text{C}^{13}] = 82$. Assuming that the clumps are spheres with radius R , we obtained the average H_2 densities and the virial parameters of the clumps.

2-D dendrograms in Position-Position plane were applied to SCUBA-2 850 μm image with setting the parameters of the minimum detection level to $2\sigma_{rms}$ ($1\sigma_{rms} \sim 0.06\text{ Jy/beam}$), the minimum increment to $2\sigma_{rms}$ and the minimum structure size to 9 pixels (3×3 pixels, corresponding to 0.86 beam size). And the minimum peak value is set to $3\sigma_{rms}$ to obtain the accurate leaves. As a result, a total of 22 dense cores were extracted from the image using the technique. All clumps and cores are presented in Figure 8.

Assuming a gas-to-dust ratio of 100, the beam-averaged H_2 column densities of the cores can be calculated from the integrated flux

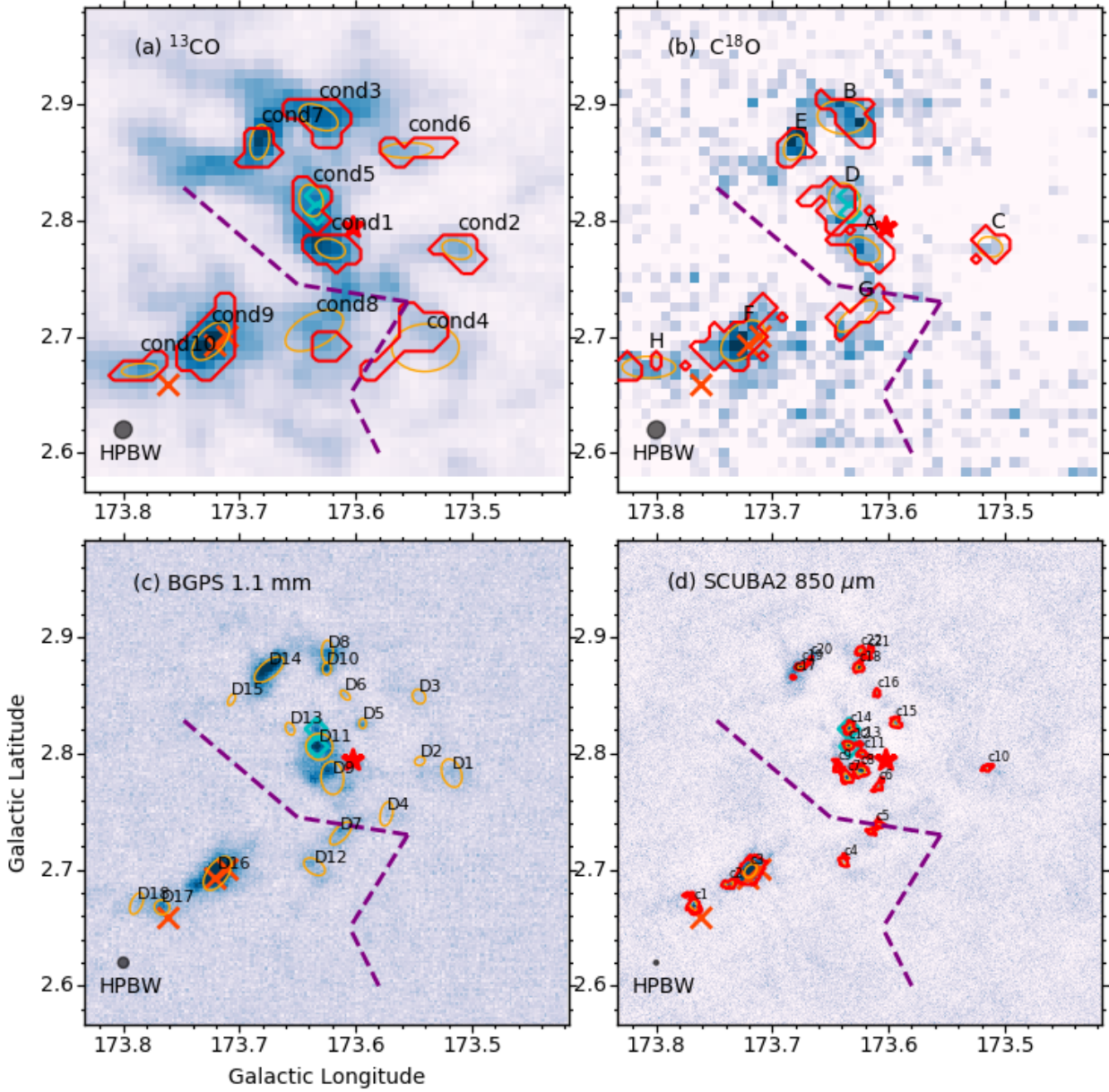


Figure 8. Clumps and cores identification in the S235 complex. (a) the ^{13}CO molecular clumps identified by using dendrogram. The red polygons indicate the dense leaves in dendrogram which were fitted by the orange ellipses. (b) the C^{18}O molecular clumps. (c) the BGPS dust clumps at 1.1 mm from Rosolowsky et al. (2010). (d) the SCUBA-2 dust cores at 850 μm .

densities of the SCUBA-2 850 μm dust emission using the following formula:

$$N(\text{H}_2) = \frac{100F_\nu}{\mu m_H \kappa_\nu B_\nu(T_d) \Omega_{beam}}, \quad (1)$$

where F_ν is the flux density, $\mu = 2.8$ is the mean molecular weight, m_H is the mass of a hydrogen atom, κ_ν represents the dust opacity per unit mass at 850 μm , which is interpolated from Ossenkopf & Henning (1994) by $\kappa_\nu = \kappa_{230} \left(\frac{\nu}{230 \text{ GHz}}\right)^\beta$, in which $\kappa_{230} = 0.9 \text{ cm}^2 \text{ g}^{-1}$

is the opacity at 230 GHz and β is the dust emissivity spectral index which is set to be 2, thus κ_ν at 850 μm is taken to be $0.21 \text{ cm}^2 \text{ g}^{-1}$, $B_\nu(T_d)$ is the Planck function, in which T_d is dust temperature and is assumed to be 20 K, Ω_{beam} is the beam solid angle. The total mass of dust cores is derived from the integrated flux density over the target:

$$M_{dust} = \frac{100D^2 S_{int}}{\kappa_\nu B_\nu(T_d)}, \quad (2)$$

where D is the distance, and S_{int} is the integrated $850 \mu\text{m}$ flux density. The physical properties of the identified dust cores are listed in Table 4. The core mass ranges from 5.5 to $31.1 M_{\odot}$, with an extra core with extreme high mass of $269 M_{\odot}$ (c3, which is located in the massive gas clump cond9). We also used the same method to calculate the beam-averaged column density and the dust clump mass for the 18 BGPS 1.1 mm dust clumps from Rosolowsky et al. (2010) found in the S235 region and then reproduced the properties catalog in Table 5.

As mentioned above, the clumps and cores were identified with four tracers of ^{13}CO , C^{18}O , BGPS 1.1 mm and SCUBA-2 $850 \mu\text{m}$, and each tracer represent different aspect of ISM, for example, optical thin ^{13}CO can trace total molecular gas, and C^{18}O with low abundance can trace high dense gas, and long wavelength dust emission can trace dense gas as well. Since cores with smaller scale are substructure of clumps, hence, each clump can be resolved into several cores. The counterpart objects (i.e., C^{18}O clumps in Table 3, SCUBA-2 cores in Table 4 and BGPS clumps in Table 5) associated to the ^{13}CO clumps are given in Table 6. Most of ^{13}CO clumps hold $1 \sim 4$ cores, only two clumps with no core inside. There are four ^{13}CO clumps namely cond5, cond7, cond9 and cond10 harbor Massive Young Stellar Objects (MYSOs), indicating massive star formation toward there.

3.4 Star formation in S235

3.4.1 Identification of young stellar objects

Low-mass young stellar objects (YSOs) can be classified as Class I, Class II and Class III objects according to their spectral indices (e.g., Evans et al. 2009). Different classes represent different evolutionary stages of YSOs, for Class I sources as the youngest protostars host circumstellar disks and infalling envelopes and Class II sources host optically thick disks, while Class III sources are the diskless pre-main-sequence stars. The YSOs with dusty circumstellar disks will cause infrared excess on their infrared colors. Many authors (e.g., Gutermuth et al. 2009; Koenig et al. 2012; Koenig & Leisawitz 2014), therefore, used NIR and MIR color excess schemes to find YSO populations. In this study, we employed UKIDSS-GPS NIR data and *Spitzer*-IRAC/MIPSGAL MIR data for finding deeply embedded and faint YSO sources. Similar work (Dewangan et al. 2016) has been done toward the S235 region. However, their survey region was only limited to the S235-Main region, in addition to the S235-ABC region. Thus we employed the systematic YSO identification methods toward the entire S235 region. And a more elaborative description of these methods is given below.

Five independent methods are employed to select YSOs and its candidates in the present work. The first method is only based on the *Spitzer*-IRAC data, and the details of criteria are given in Gutermuth et al. (2009) Phase 1 (hereafter the method 1). The method was applied to the sources that have detections in all four *Spitzer*-IRAC bands with high quality ($\sigma < 0.2\text{mag}$). First of all, we removed the extragalactic sources such as active star-formation galaxies, as their strong PAH-feature emission will cause spurious color excess in 5.8 and $8.0 \mu\text{m}$ bandpasses (Stern et al. 2005) thus can be eliminated from our sample. The other extragalactic source contamination comes from broad-line AGN which have consistent MIR colors with YSOs (Stern et al. 2005). We utilized the $[4.5]$ vs. $[4.5]-[8.0]$ color-magnitude diagram to flag and remove AGN candidates as described in Gutermuth et al. (2009). In addition, we removed sources classified as knots of shock emission and PAH-contaminated apertures. After removing the contaminant sources, using the $[3.6]-[4.5]$ vs.

$[4.5]-[5.8]$ color-color diagram, Class I young stellar objects can be identified by the following criteria,

$$\begin{aligned} [3.6] - [4.5] &> 0.7 \\ [4.5] - [5.8] &> 0.7 \end{aligned} \quad (3)$$

On the other hand, for Class II sources, the $[3.6]-[5.8]$ vs. $[4.5]-[8.0]$ color-color diagram is used, and the criterion are,

$$\begin{aligned} [3.6] - [5.8] + \sigma &\leq \frac{0.14}{0.04} \times ([4.5] - [8.0] - \sigma - 0.5) + 0.5 \\ [3.6] - [5.8] - \sigma &> 0.35 \\ [4.5] - [8.0] - \sigma &> 0.5 \\ [3.6] - [4.5] - \sigma &> 0.15 \end{aligned} \quad (4)$$

Where σ corresponds to the error of each color.

As a result, we found 194 YSO candidates, of which 22 are Class I and 172 are Class II (see Figure 9a.), and eliminated 378 PAH-rich galaxies, 400 AGN candidates, 1 knot of shock emission, and 266 PAH-contaminated apertures in the S235 region.

In method 2, we considered the sources that lack detection on either 5.8 or $8.0 \mu\text{m}$, but have high quality ($\sigma < 0.1\text{mag}$) UKIDSS-GPS JHK bands (when J band is not available, H and K bands). The classification scheme was described in Gutermuth et al. (2009) Phase 2. The method utilizes the dereddened color-color space $[K - [3.6]]_0$ vs. $[[3.6] - [4.5]]_0$ to identify YSOs because line-of-sight extinction and intrinsic variability can cause a reddened Class II source be misclassified as a Class I source. The extinction was measured by baseline colors based on the Classical T Tauri Star (CTTS) locus of Meyer et al. (1997) and standard dwarf star colors (Bessell & Brett 1988) and the color excess ratios reported in Flaherty et al. (2007). The measured colors were dereddened according to the reddening law by Flaherty et al. (2007). With the above steps, the reddened Class II candidates can be separated from the Class I candidates. Finally, 22 Class I and 70 Class II sources were obtained from method 2 (see Figure 9b.).

After running Phase 1 and Phase 2 according to Gutermuth et al. (2009), the next step (Phase 3) was to classify deeply embedded protostars and transition disks for the sources having excess emission at $24 \mu\text{m}$. Embedded protostars are Class I candidates with bright emission at MIR wavelengths but lack emission at NIR wavelengths because they are deeply embedded in dust, while transition disks are Class II sources with significant dusty disks thus also show bright emission at MIR wavelengths. The classification criteria were given in Gutermuth et al. (2009) Phase 3. With this step, 1 embedded protostar and 12 transition disk YSOs were found toward the S235 region. They were shown in Figure 9a if they have the respective colors.

Due to the detection sensitivity limitations of IRAC $[5.8]$ and $[8.0]$ bands and the strong nebula background emission, more low-mass and low-luminosity members may be missed. Therefore, We use $H-K$ vs. $H-[3.6]$ and $H-K$ vs. $H-[4.5]$ color-color maps to search for lower mass young star objects. Details of the criteria can be found in Fang et al. (2012). Figure 9c&d show the color-color diagrams of the two methods (hereafter the method 3 and method 4), and the reddening vector is from Indebetouw et al. (2005). The classification criterion is roughly parallel to the reddening vector, and the stars above the dashed line of the criterion are diskless stars, most of which are unrelated foreground or background stars. The stars below the dashed line of the criterion have very large $H-[3.6]$ or $H-[4.5]$ color, which can not be explained by the reddening of diskless stars, indicating that these stars are young stellar object with disks, and they are simply classified into Class II YSOs. Using these two methods, we obtained 46 and 36 Class II sources respectively.

Table 2. Catalog of physical properties of ^{13}CO molecular clumps in S235.

Clump seq	Gl _{on} °	Gl _{at} °	V_{LSR} km s ⁻¹	ΔV km s ⁻¹	R_{eff} pc	Mass M_{\odot}	α_{vir}	n $\times 10^3 \text{cm}^{-3}$	\bar{N} $\times 10^{22} \text{cm}^{-2}$	C ¹⁸ O ^a clump
cond1	173.622	2.776	-21.46	1.04	0.52	423.5	0.2	10.0	5.2	A
cond2	173.513	2.775	-21.47	0.7	0.51	219.8	0.2	5.6	3.4	C
cond3	173.632	2.889	-21.02	0.93	0.67	638.7	0.1	7.3	5.4	B
cond4	173.54	2.691	-20.22	1.0	1.24	607.4	0.3	1.1	2.4	-
cond5	173.638	2.817	-20.01	0.89	0.6	399.3	0.2	6.3	4.3	D
cond6	173.555	2.86	-20.37	0.42	0.61	107.1	0.1	1.6	1.4	-
cond7	173.683	2.867	-19.17	1.22	0.56	525.2	0.2	10.0	5.6	E
cond8	173.636	2.705	-16.85	1.75	1.0	496.9	0.9	1.7	2.4	G
cond9	173.725	2.696	-16.78	1.18	0.76	948.7	0.2	7.4	5.4	F
cond10	173.786	2.671	-16.55	0.7	0.48	213.1	0.2	6.7	3.3	H

^a Labels of associated C¹⁸O clumps.**Table 3.** Catalog of physical properties of C¹⁸O molecular clumps in S235.

Clump seq	Gl _{on} °	Gl _{at} °	V_{LSR} km s ⁻¹	ΔV km s ⁻¹	R_{eff} pc	Mass M_{\odot}	α_{vir}	n $\times 10^3 \text{cm}^{-3}$	\bar{N} $\times 10^{22} \text{cm}^{-2}$	N_{MYSO}^a
A	173.622	2.775	-21.67	0.79	0.62	252.6	0.2	3.7	2.2	0
B	173.639	2.889	-21.01	1.15	0.9	510.7	0.35	2.4	2.4	0
C	173.513	2.777	-21.54	0.62	0.49	103.9	0.21	3.1	1.6	0
D	173.638	2.817	-19.98	1.09	0.73	251.6	0.51	2.2	1.6	2
E	173.682	2.863	-19.06	0.94	0.49	208.1	0.29	6.	2.2	1
F	173.725	2.697	-16.8	1.39	0.88	612.5	0.44	3.1	2.5	2
G	173.627	2.718	-17.15	0.77	0.64	153.2	0.33	2.	1.6	0
H	173.806	2.674	-16.29	1.25	0.74	298.1	0.6	2.5	2.2	1

^a Numbers of associated Massive Young Stellar Object (MYSO) candidates from [Lumsden et al. \(2013\)](#).**Table 4.** Catalog of physical properties of SCUBA-2 850 μm dust cores in S235.

Core seq	Gl _{on} °	Gl _{at} °	a "	b "	PA °	S_{int} Jy	R_{eff} pc	Mass M_{\odot}	\bar{N} $\times 10^{22} \text{cm}^{-2}$
c1	173.768	2.67	16.9	9.2	113	1.86	0.21	28.0	7.4
c2	173.737	2.687	11.2	6.3	-169	1.43	0.14	21.49	5.7
c3	173.719	2.699	20.9	13.5	51	17.85	0.28	269.0	71.0
c4	173.638	2.707	10.5	7.1	100	0.53	0.14	7.98	2.1
c5	173.611	2.736	17.5	7.7	-137	0.76	0.19	11.46	3.0
c6	173.608	2.772	12.3	5.4	57	0.61	0.14	9.21	2.4
c7	173.636	2.779	10.8	7.7	122	1.36	0.15	20.46	5.4
c8	173.624	2.785	11.5	9.0	172	1.98	0.17	29.83	7.9
c9	173.644	2.789	11.8	6.4	96	0.51	0.15	7.68	2.0
c10	173.515	2.787	9.2	4.7	-161	0.37	0.11	5.59	1.5
c11	173.622	2.799	12.3	4.8	161	0.68	0.13	10.26	2.7
c12	173.634	2.807	7.9	6.2	157	1.66	0.12	25.0	6.6
c13	173.625	2.808	5.7	3.4	173	0.37	0.07	5.52	1.5
c14	173.634	2.822	9.1	7.3	61	1.22	0.14	18.32	4.8
c15	173.594	2.826	8.7	7.4	138	0.86	0.13	12.99	3.4
c16	173.61	2.852	6.5	4.7	89	0.36	0.09	5.43	1.4
c17	173.682	2.865	3.8	3.0	177	0.39	0.06	5.9	1.6
c18	173.625	2.874	8.1	6.7	66	1.5	0.12	22.6	6.0
c19	173.675	2.875	10.1	4.9	-166	2.07	0.12	31.15	8.2
c20	173.667	2.88	7.7	2.5	67	0.64	0.07	9.68	2.6
c21	173.617	2.886	11.4	6.0	50	0.85	0.14	12.79	3.4
c22	173.624	2.888	7.7	5.5	-143	0.77	0.11	11.68	3.1

Table 5. Catalog of physical properties of BGPS dust cores in S235.

Core seq	Gl _{on} °	Gl _{at} °	a "	b "	PA °	S _{int} Jy	R _{eff} pc	Mass M _⊙	\bar{N} ×10 ²² cm ⁻²
D1	173.517	2.783	45.08	29.59	70	1.34	0.32	58.2	2.7
D2	173.545	2.793	16.42	12.97	159	0.19	0.13	8.4	0.4
D3	173.545	2.849	23.47	19.09	58	0.44	0.18	19.0	0.9
D4	173.573	2.748	38.02	18.81	103	0.55	0.23	23.8	1.1
D5	173.594	2.826	15.44	11.19	91	0.48	0.11	20.9	1.0
D6	173.609	2.85	18.69	10.01	44	0.22	0.12	9.4	0.4
D7	173.613	2.731	44.98	19.94	133	1.95	0.26	84.3	4.0
D8	173.624	2.887	35.62	17.57	89	2.09	0.22	90.4	4.2
D9	173.62	2.779	51.09	34.89	85	5.13	0.37	222.0	10.0
D10	173.625	2.873	19.33	13.6	91	1.04	0.14	45.1	2.1
D11	173.631	2.806	41.67	40.84	17	5.98	0.36	258.8	12.0
D12	173.635	2.703	36.4	22.23	33	1.43	0.25	61.9	2.9
D13	173.656	2.821	20.0	13.36	66	0.26	0.14	11.0	0.5
D14	173.674	2.872	54.88	25.34	141	6.77	0.33	293.0	14.0
D15	173.707	2.846	19.37	9.34	116	0.17	0.12	7.2	0.3
D16	173.719	2.697	60.35	31.63	126	15.15	0.38	656.0	31.0
D17	173.767	2.668	23.77	22.38	24	1.62	0.2	70.2	3.3
D18	173.789	2.671	35.29	17.39	113	0.99	0.22	42.9	2.0

Table 6. Catalog of objects associated to the ¹³CO clumps.

Cond. seq	Gl _{on} °	Gl _{at} °	C ¹⁸ O clump	BGPS clump	SCUBA-2 core	N _{MYSO}	MST YSO group	Young star ^a cluster
cond1	173.622	2.776	A	D9	c6, c7, c8, c9	0	M5	-
cond2	173.513	2.775	C	D1	c10	0	M2	FSR 784
cond3	173.632	2.889	B	D8, D10	c18, c21, c22	0	M4	S235 E2
cond4	173.54	2.691	-	D4	-	0	-	-
cond5	173.638	2.817	D	D11, D13	c11, c12, c13, c14	2	M3	S235 Cl., CBB 2
cond6	173.555	2.86	-	D3	-	0	-	-
cond7	173.683	2.867	E	D14, D15	c17, c19, c20	1	M1	KKC 11
cond8	173.636	2.705	G	D7, D12	c4, c5	0	M6	-
cond9	173.725	2.696	F	D16	c2, c3	2	M7 north	BDSB 72, 73, S235B Cl.
cond10	173.786	2.671	H	D17, D18	c1	1	M7 south	BDSB 71

^a Names of associated young star clusters from [Camargo et al. \(2011\)](#).

Because UKIDSS-GPS is much more sensitive than *Spitzer*-IRAC, there are many faint YSOs ignored by IRAC but visible on UKIDSS. Therefore, we further use the UKIDSS-NIR color-color diagram (H–K vs. J–H) to search these sources. Note that the YSOs found by this method are not particularly reliable, because the SED of YSO has not reached its peak on this band, and its infrared color excess cannot very well reflect the properties of YSO disk. Therefore, we only take the stars identified by this method as the candidates for YSO. The NIR YSOs classification method was described in [Sugitani et al. \(2002\)](#) and [Dewangan et al. \(2016\)](#) (hereafter the method 5). They divided the color-color diagram into three different regions, namely "P", "T" and "F", according to the reddening bands of the Classical T Tauri (CTTS) locus ([Meyer et al. 1997](#)) and the main-sequence and giants locus ([Bessell & Brett 1988](#)). The left panel of Figure 10 shows the color-color diagram of YSO candidates identified by this method. The reddening vectors are calculated from the extinction law of [Indebetouw et al. \(2005\)](#). "P" region represents the protostellar dominated region where the sources distributed in this region may be classified as Class I sources. "T" sources are located in the reddening bands of the CTTS locus thus were classified as Class II sources. "F" sources are falling between the reddening bands of the main-sequence and giant stars locus, which are considered to be

field stars. By employing method 5, we obtained 32 Class I and 137 Class II sources.

As a result of the five methods mentioned above, we totally found 550 YSOs and candidates, of which 77 are Class I and 473 are Class II sources (12 transition disks are included). And the spatial distribution of all YSOs is shown in the right panel of Figure 10. It is uncertain whether an individual YSO is associated with S235, since there is no distance information for it. However, in our YSO catalog, the sources classified as Class I are distributed over the dense molecular clumps, so most of them are likely to associated with S235. On the other hand, the sources classified as Class II are distributed, and could be contaminated by field stars or extragalactic objects. Therefore, we use the MST clustering method to obtain YSO groups that are associated with S235.

3.4.2 MST clustering analysis of YSOs

A study of nearby cloud complexes indicates that young embedded clusters account for a significant (70-90%) fraction of all stars formed in GMCs ([Lada & Lada 2003](#)). The S235 complex, as a part of GMC G174+2.5, was found to host at least 9 embedded star clusters ([Camargo et al. 2011](#)). Clustered YSOs as the newborn members of

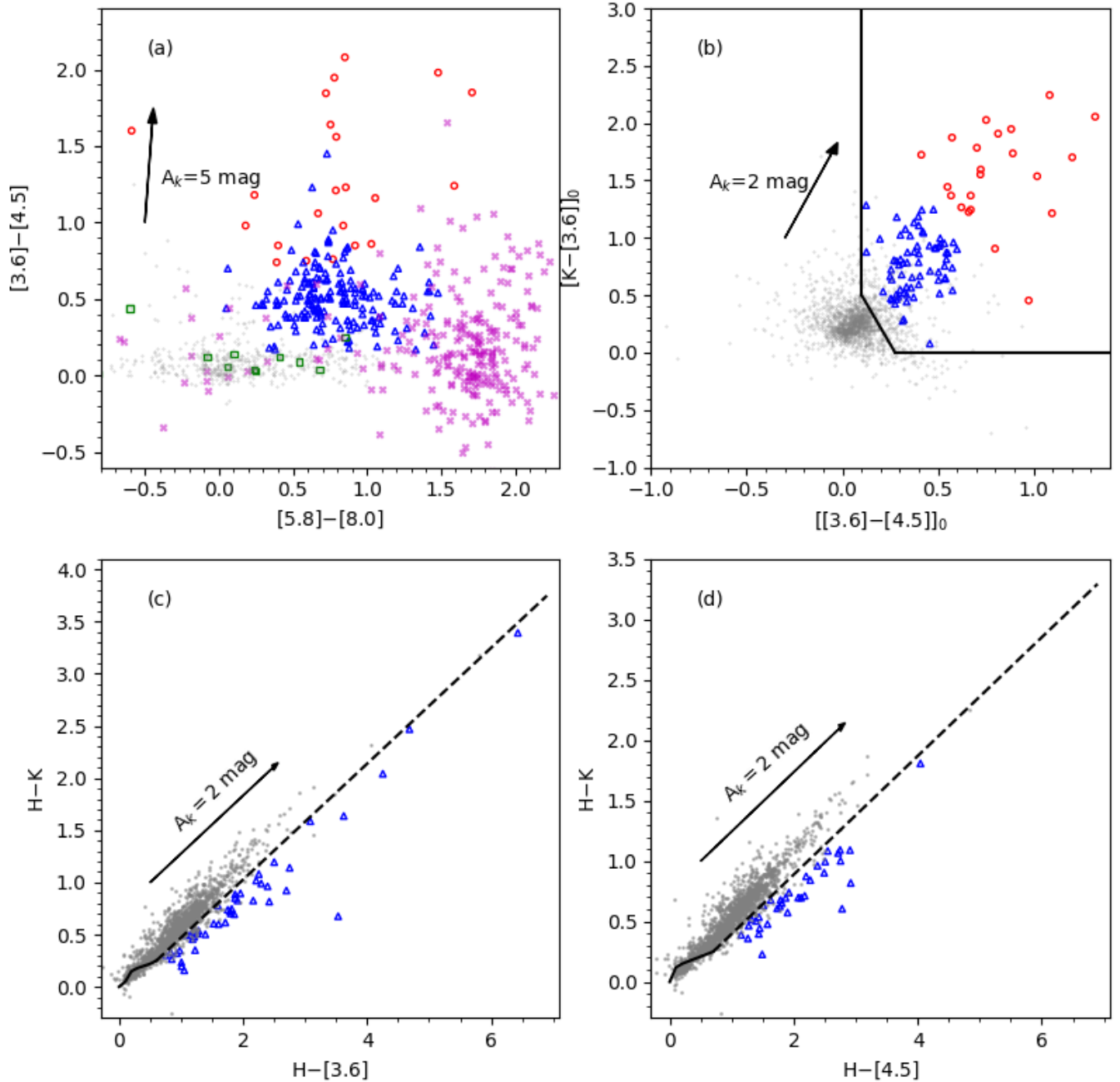


Figure 9. YSOs identification schemes from method 1–4 (represent to a–d, respectively). (a) *Spitzer*-IRAC color-color diagram ($[3.6]-[4.5]$ vs. $[5.8]-[8.0]$) (from [Gutermuth et al. 2009](#), Phase 1). (b) The deredened color-color diagram ($[K-[3.6]]_0$ vs. $[[3.6]-[4.5]]_0$) using UKIDSS-GPS and *Spitzer*-IRAC data (from [Gutermuth et al. 2009](#), Phase 2). (c) $H-K$ vs. $H-[3.6]$ color-color diagram (from [Fang et al. 2012](#)). And the solid line represent the locus of the diskless stars. (d) Same with (c) but in $H-K$ vs. $H-[4.5]$ color-color diagram. For all panels, the red circles, blue triangles and green squares represent the Class I, Class II sources and Transition disks, respectively. The magenta crosses represent the contamination from PAH-rich galaxies, AGN galaxies, knots of shocked and PAH apertures. The arrows represent reddening and K-band extinction.

young embedded star clusters thus are a good tracer of active star formation subregions in the molecular cloud. We utilized the Minimal Spanning Tree (MST) clustering method (e.g., [Barrow et al. 1985](#)) to analyze the star formation substructure in the S235 region, such as groups/clusters of YSOs ([Gutermuth et al. 2009](#); [Saral et al. 2015, 2017](#); [Sun et al. 2022](#)). MST is a unique network of a set of points (YSOs), in which the total length of the network is mini-

mized and without closed loops. The clustering method extracts YSO groups/clusters by pruning an MST with a maximum cutoff distance (d_c) and a minimum number of members (N) in a group.

There is no robust way to determine a cutoff distance for separating MST groups from "noise" YSOs, because the surface density profiles, fractions of members of YSOs, incompleteness of YSOs identification and heliocentric distance uncertainties vary from re-

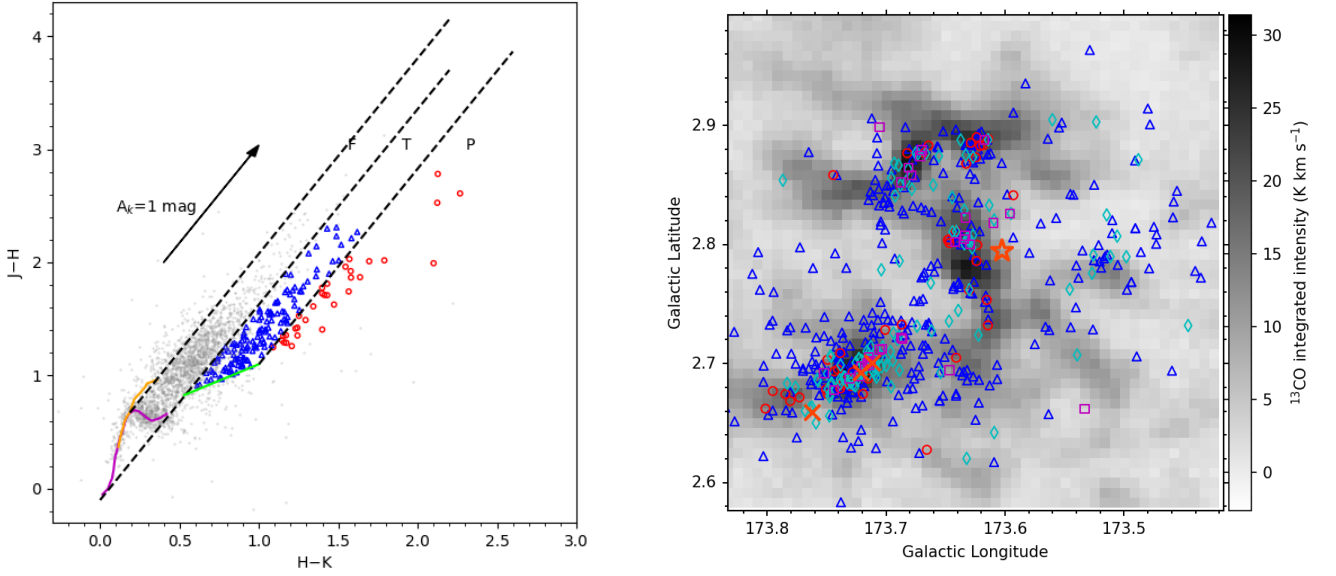


Figure 10. Left panel: JHK Young Stellar Object (YSO) candidates identification scheme from method 5. The solid curves represent the unreddened locus of main-sequence stars (magenta) and giants (orange) from [Bessell & Brett \(1988\)](#), and Classical T Tauri (CTTS) stars (green) from [Meyer et al. \(1997\)](#). The extinction vector is drawn from [Indebetouw et al. \(2005\)](#) extinction laws. The red circles represent Class I YSO candidates while the blue triangles represent Class II YSO candidates. Right panel: Spatial distribution of all YSOs and its candidates, with ^{13}CO integrated intensity map in the background. The red circles represent Class I YSOs and the blue triangle represents Class II YSOs from method 1 to 4. The magenta squares represent Class I YSO candidates while the cyan diamonds represent Class II YSO candidates from method 5.

gions to regions. The simplest way is to directly use the average length $\langle l \rangle$ of MST branches as the cutoff distance (i.e., $1 \sim 3$ times of $\langle l \rangle$, as did in [Barrow et al. 1985](#)). Although this method has its advantage in detecting YSO groups, the thresholds they adopted are arbitrary. [Gutermuth et al. \(2009\)](#) constructed the Straight Line Fit (SLF) method to identify the local surface density threshold. The SLF method use straight lines to fit the short and long branch length domain of the cumulative distribution function of the MST branch lengths, and then choose the point of intersection as the threshold distance. More details were described in [Gutermuth et al. \(2009\)](#) and [SaraI et al. \(2015\)](#).

Using the methods explained above, we performed the MST clustering analysis toward the sample of 550 YSOs we identified in S235. We first determined a cutoff distance (d_c) of MST branch lengths by employing the SLF method (see Figure 11a.), and then used a standard value of $N = 10$ as the minimum number of group members to identify YSO groups/clusters. In order to investigate how the number of identified groups changes with the minimum number of group members and the cutoff distances, we repeated the analysis with a set of test minimum numbers of group members in a range of $N = 3 \sim 18$ when $d_c = 33.7''$ (see Figure 11b.), and a set of test cutoff distances in a range of $d_c = 1'' \sim 200''$ in steps of $1''$ when $N = 10$ (see Figure 11c.), respectively.

In Figure 11a, the intersection of the two straight fitting lines indicates a cutoff distance of $33.7''$ (~ 0.25 pc at the distance of 1.55 kpc). When involved cutoff distance into the MST analysis, the number of identified MST groups monotonously decreases with the minimum number of group members as shown in Figure 11b. Such distribution can be separated into three regions. In region 1 ($3 \leq N \leq 8$), the numbers of identified groups rapidly decrease

Table 7. Properties of the MST YSO groups.

Name	Glon °	Glat °	N_{IR}	I	II	II/I	Diameter '' (pc)
M1	173.684	2.861	45	8	37	4.63	158 (1.19)
M2	173.518	2.786	10	0	10	-	58 (0.44)
M3	173.635	2.808	38	11	27	2.45	128 (0.96)
M4	173.624	2.880	31	8	23	2.88	104 (0.78)
M5	173.635	2.764	10	1	9	9.00	44 (0.33)
M6	173.641	2.695	14	2	12	6.00	84 (0.63)
M7	173.724	2.700	201	33	168	5.10	296 (2.22)

as the number of group members slightly increase, which suggests that small groups are significantly affected by contamination which accidentally have similar number of group members as small groups. In region 2 ($8 \leq N \leq 15$), the number of identified groups slightly decreases from nine groups to four groups, suggesting that groups or subgroups can be identified within this region, and the smallest group should contain at least 8 group members. Within this region, the number of groups keep steady and seven groups were identified with $N = 10$, suggesting that the standard value of $N = 10$ is good to identify substructures of YSO distribution in our study. In region 3 ($N \geq 15$), four large groups remain unchanged. Given the standard value of $N = 10$ in the MST analysis (Figure 11c), the number of groups changed as a crescent function with a set of cutoff distances and finally 7 groups were identified with the cutoff distance of $d_c = 33.7.0''$. Note that the identified group number reaches its maximum of 8 groups/subgroups when setting the cutoff distance in

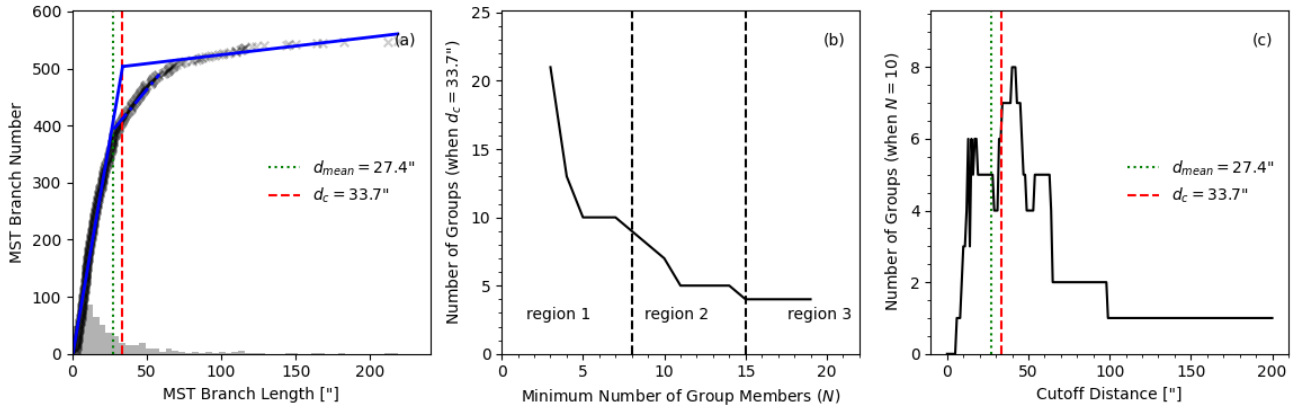


Figure 11. MST clustering analysis of YSOs. (a) The SLF method (from Gutermuth et al. 2009). The black solid line and crosses indicate the cumulative distribution function of the MST branch lengths, while the two blue solid lines fit the shot and long branch length domain, respectively. The red dashed line represents the intersection of the two fitting lines, giving the cutoff distance of $d_c = 33.7''$. The green dotted line represents the average branch length. (b) The number of identified groups change with the minimum number of group members. (c) The number of identified groups changes with the separating distance.

a range of $40'' \sim 48''$ which is longer than the cutoff distance given by SLF method.

To conclude, with both $N = 10$ and $d_c = 33.7''$ parameters involved in our MST analysis, we identified 7 MST groups which contains 63% (349/550) of the total numbers of YSOs in the S235 region. The MST groups consist of 10 – 201 YSOs with diameters of 0.33 – 2.22 pc. The spatial distribution of the MST groups is shown in Figure 12 and their properties are tabulated in Table 7.

As shown in Figure 12, the YSOs are clustering toward the star formation subregions, and most of them are still embedded in molecular gas. The spatial distribution of the bridge feature is drawn in white contours in the Figure 12b&c&d, which represents the morphology of the collisional influenced gas. The bridge feature only distribute at the southern and southeastern part of the S235 complex as separated by the blue dashed line in the figure, suggesting that the star formation activities are seriously affected by the CCC process in the southern regions but quiet in the northern regions. Considering the colliding interface and the distribution of the bridge feature, the colliding vector of the two clouds should be pointing from the south to the north (depicted as the red arrow), which is perpendicular to the blue dashed line in Figure 12b. There are at least five MST groups (M1, M3, M5, M6 and M7) associated with the bridge feature, suggesting that the star formation in these sites might be triggered by the CCC process. The zoomed-in regions of these YSO groups is shown in Figure 12c&d. The YSO group M1 (namely the YSO Wall) and M7 show a elongated shape with a length of ~ 2 pc and ~ 3 pc, respectively. On the other hand, the bridge feature distribution also shows a close shape to the YSO group, indicating that the YSOs (at least the Class I YSOs) in these MST groups (or young star clusters) may form from the dense gas compressed by CCC process.

3.5 The effect of cloud-cloud collision on star formation

Our systematically census of young stellar objects suggested that the S235 complex is a very active star formation region with a wide mass range of young stellar populations clustering in seven subregions. we obtained the core formation efficiency (CFE), the star formation efficiency (SFE) and rate (SFR) by counting the number of dust cores and YSOs in each ^{13}CO molecular clump. The CFE or SFE is defined

as below,

$$\text{CFE (SFE)} = \frac{M_x}{M_x + M_{\text{cloud}}}, \quad (5)$$

where M_x is the total mass of cores (CFE) or stars (SFE) and M_{cloud} is the total cloud mass. CFE and SFE indicate the fraction of molecular gas evolved into dense cores and stars. SFE varies from less than 0.1% to 50% among molecular clouds with a median value of 2% in the inner Galaxy (Myers et al. 1986).

As mentioned earlier, only the Class I and Class II YSO candidates were identified by our NIR-MIR YSO selection scheme, so that we could not calculate the total stellar mass of each ^{13}CO clump directly due to the lack of information on the number of the evolved stars (Class III and main-sequence stars) and the mass of each star. Therefore, we made the following assumptions in calculation: (1) A disk fraction ($N(\text{II})/N(\text{II}+\text{III})$) is considered to be 50% (Fang et al. 2013; Gong et al. 2016), given $N(\text{III}) = N(\text{II})$. (2) The mass distribution of YSOs follows the initial mass function (IMF) of Chabrier (2003). (3) Accept a lower magnitude limit of the identified YSOs in K band to 14 mag, which corresponds to 3.05 absolute magnitude at the distance of 1.55 kpc. This gives the lower mass limit of $0.03 M_{\odot}$ (Siess et al. 2000). We also simply assumed the upper limit of the IMF to be $80 M_{\odot}$ (Gong et al. 2016), because the number of massive stars decrease seriously in IMF thus will not affect the total mass significantly. Taking these assumptions into account, one can calculate the total stellar mass by integrating the IMF. In addition, this result should also be added to the mass of the Massive Young Stellar Objects (MYSOs) as its final total stellar mass, and we assume that the average mass of each MYSO is $10 M_{\odot}$. The calculation results are listed in Table 8. To conclude, the average mass of YSOs is about $0.64 M_{\odot}$ which is in agreement with observations. The CFE for each ^{13}CO clump ranges from 2.5% to 23.4%, while the SFE is in a range of 2.9% – 21.2% which is greater than the SFE (3.0%– 6.3%) in nearby clouds (Evans et al. 2009) and the median value (2%) in the inner Galaxy (Myers et al. 1986). Note that we only counted the YSOs who are the members of the MST groups as well as enclosed by the area of a clump, so that some clumps did not present SFE even though they harbors some scattered YSOs. The uncertainties of CFE and SFE are estimated by the error from gas mass (40% of gas mass (Beaumont et al. 2013)) and the error from YSO mass (Poisson error $\sqrt{N}/N \times M_{\star}$).

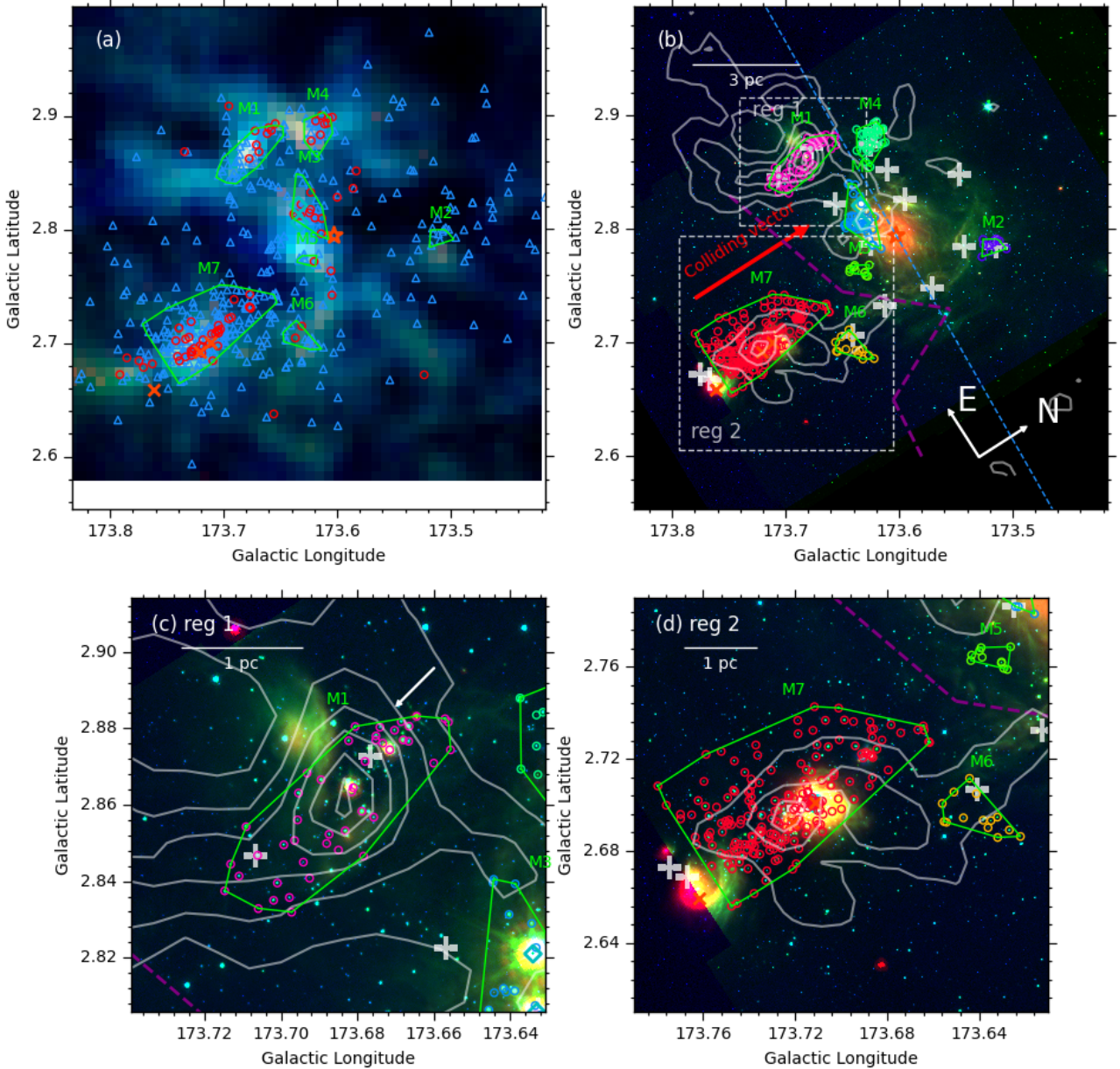


Figure 12. Distribution of the MST YSO groups. (a) The distribution of all YSOs with MST groups. The background image is the CO color composite image, in which blue is ^{12}CO , green is ^{13}CO , and red is C^{18}O . The red circle represents Class I and the blue triangle represents Class II. (b) The color composite image is coding from MIPS $24\ \mu\text{m}$ (Red), IRAC $4.5\ \mu\text{m}$ (Green) and UKIDSS-GPS K band (Blue). The circles in different colors represent different YSO groups which are also highlighted by the green polygons. The white crosses indicate the BGPS 1.1 mm dust clumps. The white contours represent the ^{13}CO distribution of the bridge feature (integrated from $-17.5 \sim -19.5\ \text{km s}^{-1}$). The contours start from $3\ \text{K km s}^{-1}$ ($3\ \sigma$) to $21\ \text{K km s}^{-1}$ in steps of $3\ \text{K km s}^{-1}$. The magenta dashed line represents the colliding interface found by the moment 2 map. The blue dashed line divides the S235 complex into two parts. The southern part was strongly affected by CCC process while the northern part was collision quiet. And the red arrow indicates the colliding vector from the south to the north. (c) and (d) The zoomed-in regions of M1 and M7 from (b).

After calculating the stellar mass toward each ^{13}CO clump, we can directly derive the SFR by,

$$\text{SFR} = \frac{M_{\star}}{\tau}, \quad (6)$$

where τ is the average age of YSOs assumed to be 2 Myr (Evans et al. 2009). The SFRs varies from 6.4 to $127.5\ M_{\odot}\ \text{Myr}^{-1}$ among the clumps. Three clumps (cond5, cond7 and cond9) with high values of SFR (30.7 , 31.1 and $127.5\ M_{\odot}\ \text{Myr}^{-1}$, respectively) are associated

Table 8. Catalog of derived properties of ^{13}CO clumps in S235.

Cond. seq	Gl _{on} °	Gl _{at} °	R _{eff} pc	M _{gas} M _⊙	M _{cores} M _⊙	CFE %	N _{YSOs} I+II	N _{MYSOs}	M _{stars} M _⊙	SFE %	SFR M _⊙ /Myr
cond1	173.622	2.776	0.52	423.5	67.2	13.7±6.7	0+10	0	12.7	2.9±1.3	6.4
cond2	173.513	2.775	0.51	219.8	5.6	2.5±1.4	0+10	0	12.7	5.5±2.4	6.4
cond3	173.632	2.889	0.67	638.7	47.1	6.9±3.6	8+23	0	34.4	5.1±2.0	17.2
cond4	173.54	2.691	1.24	607.4	-	-	0	0	-	-	-
cond5	173.638	2.817	0.6	399.3	59.1	12.9±6.4	11+27	2	61.4	13.3±4.8	30.7
cond6	173.555	2.86	0.61	107.1	-	-	0	0	-	-	-
cond7	173.683	2.867	0.56	525.2	46.8	8.2±4.2	8+37	1	62.2	10.6±3.9	31.1
cond8	173.636	2.705	1.0	496.9	19.5	3.8±2.1	2+12	0	16.6	3.2±1.4	8.3
cond9	173.725	2.696	0.76	948.7	290.5	23.4±10.2	33+168	2	255.0	21.2±6.7	127.5
cond10	173.786	2.671	0.48	213.1	28.0	11.6±5.8	5+13	1	29.7	12.2±4.7	14.9

with the M3, M1 and M7 YSO groups, in which the star formation are possibly triggered by collision.

When drawing the spatial distribution of CFE and SFE for the ten ^{13}CO clumps (see Figure 13a), the S235 complex can also be divided into two subregions (the South and the North) as it has been shown in Figure 12b by a blue dashed line. We also plotted the CFE and SFE profiles of the complex along the colliding vectors from the south to the north in terms of the identified ^{13}CO clumps (see Figure 13b). 4/6 of the clumps in the southern subregion present higher CFE and SFE larger than 10% with a mean value of 12.3% and 10.6%, respectively. However, all of the clumps in the northern subregion host lower CFE and SFE with an average value of 2.4% and 2.6%, respectively. Note that the star formation in the southern subregion is seriously affected by the CCC process, while the northern subregion is influenced by the expansion of the S235 HII region, indicating that the CCC process can significantly enhance the CFE and SFE of the clouds by 3 ~ 5 times larger than that of the clouds without collision influence.

As mentioned above, our present work supports that the cloud-cloud collision process might have taken place in the S235 complex. The most direct evidence of cloud-cloud collision is that the two clouds meet at the same position with a supersonic relative speed. S235 is consistent with this scenario, as shown in Figure 14, the S235-Main (1547^{+44}_{-43} pc) and S235-ABC (1567^{+33}_{-39} pc) are nearly located at the same position within 1σ error range, indicating that they are in contact with each other. On the other hand, the S235-Main is approaching us at a blue-shifted velocity of -20.5 km s^{-1} , while the S235-ABC is at a slower blue-shifted velocity of -16.5 km s^{-1} , indicating that the cloud-cloud collision process has occurred in S235 or the two clouds are currently moving away from each other. This result is consistent with the observational signatures of cloud-cloud collision process, such as the broad bridge feature connecting the two clouds with a supersonic separating velocity, the distinct complementary distribution of the two clouds and the broad line widths of CO emission in the colliding interface. As did in Dewangan & Ojha (2017), they compared the typical collision time scale (~ 0.5 Myr) with the dynamical ages of the compact HII regions in the S235-ABC (0.06–0.22 Myr) and the average ages of the YSOs (Class I of ~ 0.44 Myr and Class II of 1–3 Myr), and found that the formation of the youngest populations and massive stars might be induced by the CCC about 0.5 Myr ago. The tight association between the YSO groups (M1 and M7) and the bridge feature (collisional impact gas) also supports the conclusion.

In summary, the picture of cloud-cloud collision process in the S235 molecular cloud complex can be inferred as follows: the S235-Main and the S235-ABC began to collide with each other in about

3 ~ 5 Myr ago, triggering the formation of large amounts of low-mass, aged Class II YSOs. And then in about 0.5 Myr ago, more dense gas was compressed to form younger stellar population in groups (M1, M3, M5, M6, and M7) and massive young stellar objects (MYSOs) in M1, M3, and M7, as well as the O-type star in the S235-Main and B-type stars in S235-ABC. Finally, to the present day, the two molecular clouds may pull out of collision state and moving away from each other. In order to form massive objects, a higher CFE or SFE is required. The CCC process as a mechanism can enhance the CFE and SFE to over 10%, which is significantly (3~5 times) larger than the clouds whose star formation was triggered by the expansion of HII region or the clouds without collision influence.

4 SUMMARY

In this paper, we have performed a study of cloud-cloud collision (CCC) toward the S235 complex and its effects on triggering star formation using the CO data from PMO-13.7m telescope and the archival data. The main results are summarized as follows.

(i) we confirmed the results the cloud-cloud collision process in S235 with the observational signatures of the supersonic velocity separation ($\sim 4 \text{ km s}^{-1}$), the broad bridge feature, the colliding interface (with large velocity dispersion of $\sim 2 \text{ km s}^{-1}$) and the distinct complementary distribution between the S235-Main and the S235-ABC.

(ii) The high precision Gaia parallax measurement method was used to determine the distance of two main molecular cloud components in S235, the S235-main and the S235-ABC, which is in a distance of 1547^{+44}_{-43} pc and 1567^{+33}_{-39} pc, respectively. And their relative distance is less than the error range of 1σ , indicating that these two clouds are probably colliding with each other at the same place. Meanwhile, we used their average distance of 1552 pc as the distance of S235.

(iii) Ten ^{13}CO clumps and 22 dense cores were identified using the PMO-13.7m ^{13}CO data and SCUBA-2 data, respectively. And each clump hosts 1 ~ 4 cores with mass ranges from 5 – 270 M_{\odot} .

(iv) A total of 550 YSOs were identified, and 63% of them were clustering into 7 MST groups (M1–M7). The formation of YSOs groups (M1, M3, M5, M6 and M7), and the massive young stellar objects (MYSOs) in M1, M3 and M7 may be triggered by the CCC process, which enhance the CFE and SFE of cloud to over 10%, which is 3~5 times larger than that without the influence of collision.

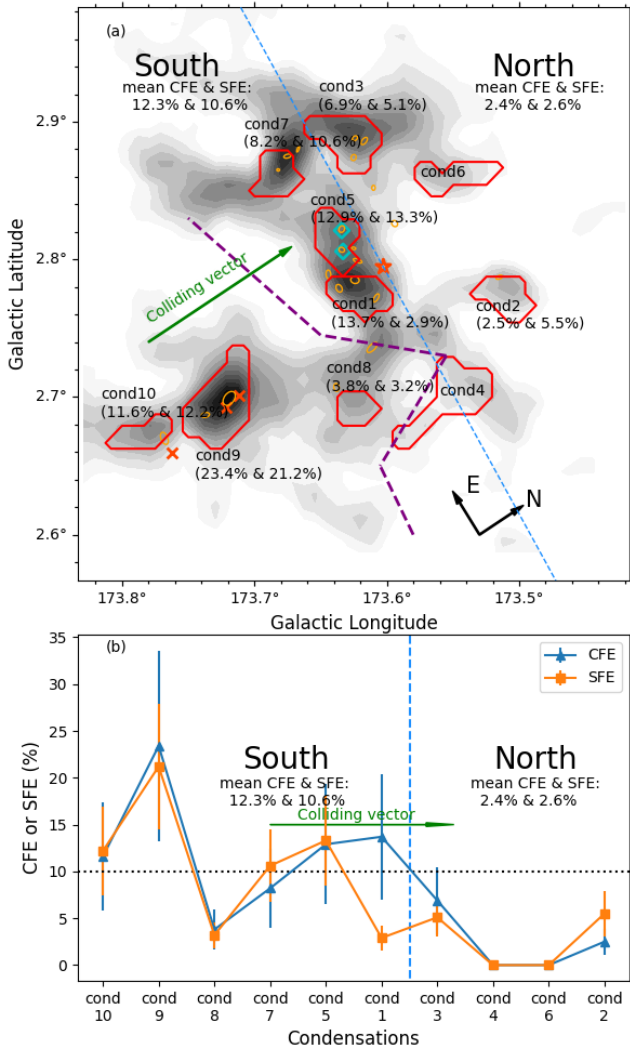


Figure 13. (a) Spatial distribution of core and star formation efficiency. The gray scale image represents the ^{13}CO data. The red polygons indicate the ^{13}CO clumps while the orange ellipses represent the SCUBA-2 dust cores at $850\ \mu\text{m}$. The values of CFE and SFE for each clump are drawn in the figure, and the first and the second number represents the CFE and SFE, respectively. The blue dashed line divides the S235 complex into two subregions, the "South" and the "North", according to the distribution of the bridge feature in Figure 12. The green arrow indicates the colliding vector which perpendicular to the blue dashed line. (b) The CFE and SFE profiles of the complex from south to north in terms of the ^{13}CO clumps. The blue and orange solid line represents the profile of CFE and the SFE, respectively. The green arrow and the blue dashed line are drawn in the same manners as in (a). The mean CFE and SFE in the southern subregion (12.3% & 10.6%) is about 3 ~ 5 times than that of in the northern sub-region (2.4% & 2.6%) of the complex.

ACKNOWLEDGEMENTS

We acknowledge support by the National Natural Science Foundation of China (NSFC, Grant No. 12041305, 12373026). This work is based on data obtained as part of the Milky Way Imaging Scroll Painting (MWISP) science project conducted by Purple Mountain Observatory (PMO). This paper made use of data products from the UKIRT Infrared Deep Sky Survey, the Two Micron All Sky Survey (a joint project of the University of Massachusetts and the

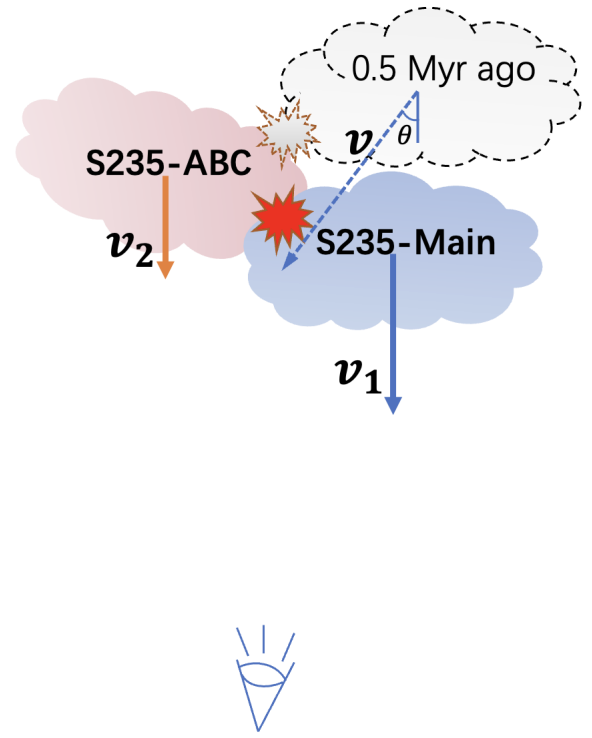


Figure 14. Cloud-cloud collision scenario in S235. The S235-Main is much closer and approaching us at a much faster speed ($4\ \text{km s}^{-1}$ relative to S235-ABC), indicate that the two molecular clouds are probably moving out of the collision state. However, both the massive young stellar objects and Class I YSOs formed before 0.5 Myr, which is the most intense moment of cloud-cloud collision. At this point, the S235-Main collided with the S235-ABC with an incident angle of θ at a colliding velocity greater than $4\ \text{km s}^{-1}$.

Infrared Processing and Analysis Center/California Institute of Technology, funded by NASA and NSF) and the archived data obtained with the *Spitzer* Space Telescope (operated by the Jet Propulsion Laboratory, California Institute of Technology under a contract with NASA). This publication made use of information from the Red MSX Source survey database which was constructed with support from the Science and Technology Facilities Council of the UK. This paper made use of the Canadian Galactic Plane Survey (supported by a grant from the Natural Sciences and Engineering Research Council of Canada). This publication made use of data products from the European Space Agency (ESA) space mission Gaia, the data from which were processed by the Gaia Data Processing and Analysis Consortium (DPAC). The Gaia Archive is reachable from the Gaia home page (<http://www.cosmos.esa.int/gaia>)

DATA AVAILABILITY

The data supporting the plots within this article are available on reasonable request to the corresponding author.

REFERENCES

- Aguirre J. E., et al., 2011, *ApJS*, 192
- Anathpindika S. V., 2010, *MNRAS*, 405, 1431
- Barrow J. D., Bhavsar S. P., Sonoda D. H., 1985, *MNRAS*, 216, 17
- Beaumont C. N., Offner S. S. R., Shetty R., Glover S. C. O., Goodman A. A., 2013, *ApJ*, 777, 173
- Bergin E. A., Tafalla M., 2007, *ARAA*, 45, 339
- Bessell M. S., Brett J. M., 1988, *PASP*, 100, 1134
- Camargo D., Bonatto C., Bica E., 2011, *MNRAS*, 416, 1522
- Chabrier G., 2003, *PASP*, 115, 763
- Chapin E. L., Berry D. S., Gibb A. G., Jenness T., Scott D., Tilanus R. P., Economou F., Holland W. S., 2013, *MNRAS*, 430, 2545
- Dempsey J. T., Friberg P., Jenness T., Tilanus R. P. J., Thomas H. S., 2013, *MNRAS*, 430, 2534
- Dewangan L. K., Anandarao B. G., 2011, *MNRAS*, 414, 1526
- Dewangan L. K., Ojha D. K., 2017, *ApJ*, 849, 65
- Dewangan L. K., Luna A., Ojha D. K., Anandarao B. G., Mallick K. K., Mayya Y. D., 2015, *ApJ*, 811, 79
- Dewangan L. K., Ojha D. K., Luna A., Anandarao B. G., Ninan J. P., Mallick K. K., Mayya Y. D., 2016, *ApJ*, 819, 66
- Dewangan L. K., Ojha D. K., Zinchenko I., 2017, *ApJ*, 851, 140
- English J., et al., 1998, *PASA*, 15, 56
- Evans & Blair G. N., 1981, *ApJ*, 246, 394
- Evans N. J., et al., 2009, *ApJS*, 181, 321
- Fang M., et al., 2012, *A&A*, 539, A119
- Fang M., Kim J. S., Boekel R. V., Sicilia-Aguilar A., Henning T., Flaherty K., 2013, *ApJS*, 207, 5
- Fazio G. G., et al., 2004, *ApJS*, 154, 10
- Flaherty K. M., Pipher J. L., Megeath S. T., Winston E. M., Gutermuth R. A., Muzerolle J., Allen L. E., Fazio G. G., 2007, *ApJ*, 663, 1069
- Frerking M. A., Langer W. D., Wilson R. W., 1982, *ApJ*, 262, 590
- Fujita S., et al., 2017, *arXiv e-prints*, p. arXiv:1711.01695
- Fukui Y., et al., 2014, *ApJ*, 780, 36
- Fukui Y., et al., 2015, *ApJ*, 807, L4
- Fukui Y., et al., 2016, *ApJ*, 820, 26
- Fukui Y., et al., 2018, *ApJ*, 859, 166
- Fukui Y., Habe A., Inoue T., Enokiya R., Tachihara K., 2021, *Publications of the Astronomical Society of Japan*, 73, S1
- Furukawa N., Dawson J. R., Ohama A., Kawamura A., Mizuno N., Onishi T., Fukui Y., 2009, *ApJ*, 696, L115
- Gaia Collaboration et al., 2016, *A&A*, 595, A1
- Gaia Collaboration et al., 2021, *A&A*, 649, A1
- Gao Y., Solomon P. M., 2004, *ApJ*, p. 20
- Georgelin Y. M., Georgelin Y. P., Roux S., 1973, *A&A*, 25, 337
- Ginsburg A., et al., 2013, *ApJS*, 208
- Gong Y., et al., 2016, *A&A*, 588, A104
- Gong Y., et al., 2017, *ApJL*, 835, 1
- Gutermuth R. a., Megeath S. T., Myers P. C., Allen L. E., Pipher J. L., Fazio G. G., 2009, *ApJS*, 184, 18
- Habe A., Ohta K., 1992, *PASJ*, 44, 203
- Hayashi K., et al., 2018, *PASJ*, 70, S481
- Henshaw J. D., et al., 2019, *MNRAS*, 485, 2457
- Herbst W., Assousa G. E., 1978, in Gehrels T., Matthews M. S., eds, IAU Colloq. 52: Protostars and Planets. p. 368
- Heyer M. H., Carpenter J. M., Ladd E. F., 1996, *ApJ*, 463, 630
- Indebetouw R., et al., 2005, *ApJ*, 619, 931
- Kazes I., Walmsley C. M., Churchwell E., 1977, *A&A*, 60, 293
- Kennicutt Robert C. J., 1998, *ApJ*, 498, 541
- Kirsanova M. S., Sobolev a. M., Thomasson M., Wiebe D. S., Johansson L. E. B., Seleznev a. F., 2008, *MNRAS*, 388, 729
- Kobayashi M. I., Kobayashi H., Inutsuka S. I., Fukui Y., 2018, *PASJ*, 70, S591
- Koenig X. P., Leisawitz D. T., 2014, *ApJ*, 791, 131
- Koenig X. P., Leisawitz D. T., Benford D. J., Rebull L. M., Padgett D. L., Assef R. J., 2012, *ApJ*, 744, 130
- Lada C. J., Lada E. a., 2003, *ARAA*, 41, 57
- Lawrence A., et al., 2007, *MNRAS*, 379, 1599
- Lumsden S. L., Hoare M. G., Urquhart J. S., Oudmaijer R. D., Davies B., Mottram J. C., Cooper H. D., Moore T. J., 2013, *ApJS*, 208
- McKee C. F., Ostriker E. C., 2007, *ARAA*, 45, 565
- McKee C. F., Tan J. C., 2003, *ApJ*, 585, 850
- Meyer M. R., Calvet N., Hillenbrand L. A., 1997, *AJ*, 114, 288
- Milam S. N., Savage C., Brewster M. a., Ziurys L. M., Wyckoff S., 2005, *ApJ*, 634, 1126
- Motte F., Louvet F., Nguyễn Lu’O’Ng Q., 2015, *Proceedings of the International Astronomical Union*, 12, 9
- Motte F., Louvet F., Nguyen Lu’O’Ng Q., 2017, Clusters of high-mass protostars: From extreme clouds to mini-bursts of star formation, doi:10.1017/S1743921316007006
- Myers P. C., Dame T. M., Thaddeus P., Cohen R. S., Silverberg R. F., Dwek E., Hauser M. G., 1986, *ApJ*, 301, 398
- Ossenkopf V., Henning T., 1994, *A&A*, 291, 943
- Peretto N., et al., 2013, *Astronomy and Astrophysics*, 112
- Rosolowsky E., et al., 2010, *ApJS*, 188, 123
- Saral G., Hora J. L., Willis S. E., Koenig X. P., Gutermuth R. A., Saygac A. T., 2015, *ApJ*, 813, 25
- Saral G., Hora J. L., Audard M., Koenig X. P., Motte F., Saygac A. T., Smith H. A., 2017, *ApJ*, 839, 108
- Shan W., et al., 2012, *IEEE Transactions on Terahertz Science and Technology*, 2, 593
- Siess L., Dufour E., Forestini M., 2000, *A&A*, 358, 593
- Skrutskie M. F., et al., 2006, *AJ*, 131, 1163
- Stern D., et al., 2005, *ApJ*, 631, 163
- Sugitani K., et al., 2002, *ApJ*, 565, L25
- Sun J., Gutermuth R. A., Wang H., Zhang S., Long M., 2022, *MNRAS*, 516, 5258
- Takahira K., Tasker E. J., Habe A., 2014, *ApJ*, 792, 63
- Takahira K., Shima K., Habe A., Tasker E. J., 2018, *PASJ*, 70, S58
- Tasker E. J., Tan J. C., 2009, *ApJ*, 700, 358
- Torii K., et al., 2011, *ApJ*, 738, 46
- Torii K., et al., 2015, *ApJ*, 806, 7
- Torii K., et al., 2017a, *PASJ*, 00, 1
- Torii K., et al., 2017b, *ApJ*, 835, 142
- Whitworth A. P., Bhattal A. S., Chapman S. J., Disney M. J., Turner J. A., 1994, *MNRAS*, 268, 291
- Wilson T. L., Rood R., 1994, *ARA&A*, 32, 191
- Wu B., Tan J. C., Nakamura F., Loo S. V., Christie D., Collins D., 2017, *ApJ*, 835, 137
- Yan Q.-Z., Zhang B., Xu Y., Guo S., Macquart J.-P., Tang Z.-H., Walsh A. J., 2019a, *A&A*, 624, A6
- Yan Q.-Z., Yang J., Sun Y., Su Y., Xu Y., 2019b, *ApJ*, 885, 19
- Zinnecker H., Yorke H. W., 2007, *ARAA*, 45, 481

This paper has been typeset from a $\text{\TeX}/\text{\LaTeX}$ file prepared by the author.